

A novel image-based ultrasonic test to map material mechanical properties at high strain-rates

R. Seghir · F. Pierron

Received: 09.02.2017 / Accepted: 13.08.2017

Abstract An innovative identification strategy based on high power ultrasonic loading together with both infrared thermography and ultra-high speed imaging is presented in this article. It was shown to be able to characterize the visco-elastic behaviour of a polymer specimen (PMMA) from a single sample over a range of temperatures and strain-rates. The paper focuses on moderate strain-rates, i.e. from 10 to 200 s⁻¹, and temperatures ranging from room to the material glass transition temperature, i.e. 110°C. The main originality lies in the fact that contrary to conventional Dynamic Mechanical Thermal Analysis (DMTA), no frequency or temperature sweep is required since the experiment is designed to simultaneously produce both a heterogeneous strain-rate state and a heterogeneous temperature state allowing a local and multi-parametric identification. This article is seminal in nature and the test presented here has good potential to tackle a range of other types of high strain-rate testing situations.

Keywords Ultra-high speed · visco-elasticity · PMMA · infrared thermography · identification

R. Seghir
Faculty of Engineering and the Environment, University of Southampton, Southampton, UK
E-mail: r.seghir@soton.ac.uk

F. Pierron
Faculty of Engineering and the Environment, University of Southampton, Southampton, UK
E-mail: f.pierron@soton.ac.uk

1 Introduction

In many instances in life, materials around or within us suffer deformation at high rates. This is the case when engineering structures undergo impact, crash, blast, etc. but also when forming materials like stamping or machining for instance. Another important area concerns biological tissues. For instance, traumatic brain injuries (TBI) involve damage of brain tissues caused by their high rate deformation following impact load of the skull. Thanks to the significant progress in computing power and computational mechanics tools, it is now possible to perform extremely detailed numerical simulations of many complex situations where materials deform at high rates, with the objective to design safer structures, assess tissue injuries or devise more effective manufacturing processes, as mentioned above. However, to deliver their full potential, these computations require the input of reliable and accurate mechanical constitutive models of the materials loaded at high strain-rates. This is an extremely challenging problem because of both the dynamic nature of the mechanical fields and the technological difficulties associated with strain metrology. Presently, this represents an important scientific bottleneck for society to fully benefit from such advances in numerical simulation.

A number of testing techniques are available to identify the high strain-rate properties of materials, as reviewed in [5]. Most of them rely on very limited experimental information, such as strain gauges or point velocity measurements with VISAR technology. As a consequence, the tests need to follow strict assumptions to relate the measurements to the material behaviour, for instance, uniform strain field and no inertia effects are typical assumptions in split Hopkinson pressure bar (SHPB) testing.

The advent of full-field optical metrology, such as digital image correlation [35] or the grid method [10], combined with the new developments in ultra-high speed imaging [29,2,36] provides a unique opportunity to revisit high strain-rate testing techniques. In particular, full-field of accelerations can be obtained which provides a powerful image-embedded load cell if the material density is known, which is usually the case. This concept was first proposed in 2009 in [22], published in full in 2011 [23], where a proof of principle experiment was performed on quasi-isotropic composite specimens, with and without a free hole. The in-plane Young's modulus and Poisson's ratio were identified satisfactorily before the onset of damage, within the first 30 μs of the test, at strain-rates up to 1000 s^{-1} . The grid method was used to measure the deformation together with a Cordin 550-62 rotating mirror ultra-high speed camera operating at 30 kfps. However, this test was performed on a tensile Kolsky bar, though the bars were not used to obtain the impact force. The concept was then extended to purely inertial tests which showed to be much more suited for this kind of analysis. The very first example dealt with concrete spalling tests [26], and was then extended to composites [27] and metals [4,3,19]. Since then, the idea has spread and several groups worldwide are starting to use

the technique [17, 14, 16, 13, 21, 40, 41].

Initially, this idea to use the full-field acceleration as a load cell with the Virtual Fields Method came from seminal work by Prof. Michel Grédiac [9, 8] using vibration tests. In this case, high speed imaging is not necessary and the acceleration derives easily from the deflection using the harmonic assumption. This was extended later on to include damping [7]. Recently, an article showed that ultrasonic excitation combined with ultra-high speed and infrared imaging [37] could be used to image the high strain-rate deformation of a polymeric foam, though the authors did not use the acceleration to identify stiffness. This was released in a later contribution [25]. The present paper builds up on this to explore the potential of this test in more depth on a homogeneous PMMA specimen. In particular, the original idea of the paper consists in investigating how heterogeneous loadings states, e.g. stationary or transient deformation waves, combined with the measurement of the local strain, strain-rate, temperature and stress (from acceleration) states can be used to identify viscoelastic material properties over a wide range of thermo-mechanical conditions. In other words, this provides a unique opportunity to identify from one single experiment, data which would have normally required a battery of tests and samples. This work is seminal in nature and focuses on the methodology rather than on the analysis of the material behaviour. However, comparison with literature results and Dynamic Mechanical Thermal Analysis (DMTA) performed on a specimen from the same material sheet enables to gain confidence in the obtained results. In addition the present data concern the moderate strain-rate range, tens to hundreds of s^{-1} , which is notoriously difficult to access with conventional servo-hydraulic machines or SPHB.

In a first part, the experimental setup and the theoretical framework are detailed. In a second part, the experimental results are presented and discussed. Finally, the identification process is simulated to provide a first idea of the optimal experimental parameters required to achieve a precise identification.

2 Experiment and data processing

2.1 Experimental setup

The concept of the experiment consists in producing within a viscoelastic sample, both a heterogeneous deformation-rate state and a heterogeneous temperature state, and capturing the thermo-mechanical response of the material through full-field measurements. To achieve this, five key elements are required, as shown in Figure 1.

A high-power ultrasonic transducer - The NextGen Lab 750 system from SynapTec (France) allows to cyclically deform the sample at 20 kHz up to a peak-to-peak displacement amplitude of 120 μm , depending on the sample

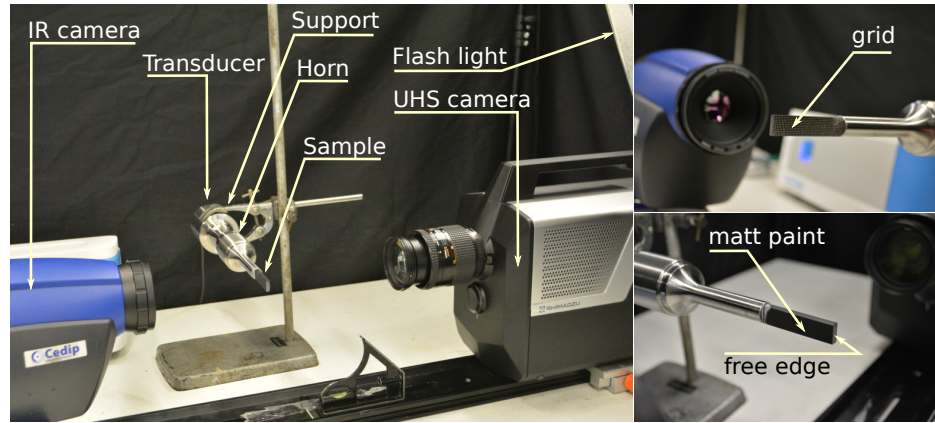


Fig. 1: Image-based DMTA experimental setup. Sample dimensions are 52 mm \times 12 mm \times 4 mm.

design and damping. The actuator is a bolt-clamped Langevin type transducer composed of a stack of piezoelectric elements resonant at 20 kHz. The displacement amplitude is boosted using a titanium horn together with the transducer, *i.e.* a mechanical amplifier. The output horn diameter, *i.e.* the active surface, is 12 mm, so that samples up to the same width can be attached to it.

A middle wavelength¹ infrared (IR) camera - The Silver 480M from Cedip (now FLIR) measures the heat flux radiated by the deforming sample and reconstructs space resolved surface temperature fields. The IR camera has a resolution of 320 \times 256 pixels, a NEDT² of about 20 mK at 25 °C, and 6000 frames can be recorded up to 383 Hz. Reducing the acquisition window down to 64 \times 12 pixels allows to reach a frame rate of 16 kHz [6]. Nevertheless, in the present experiment, the camera was used at a frame rate of 50 fps only, *i.e.* 1 frame every 400 loading cycles at 20 kHz, with an integration time of 509 μ s to cover the range 20 - 100 °C. The low frame rate was chosen to record the temperature over a long time frame, this point is detailed later on. Finally, the camera was used together with a 27 mm lens leading to a working distance of about 140 mm and a field of view of 60 \times 48 mm. An example of an IR frame captured by the camera is shown in Figure 2b. The sample is delineated by the black dotted line, its free edge is on the right while the tip of the ultrasonic horn can be seen on the left.

An ultra-high speed (UHS) camera - The HyperVision HPV-X camera from the Shimadzu Corporation (Japan) is used to capture images of the deforming sample to obtain space and time resolved displacement and acceleration³ fields. The UHS camera has a resolution of 400 \times 250 pixels and 128 frames can be recorded up to a frame rate of 5 Mfps. Here, a frame rate of 500 kfps was chosen, *i.e.* 25 frames/cycle at 20 kHz. The sensor noise was measured on

¹3-5 μ m

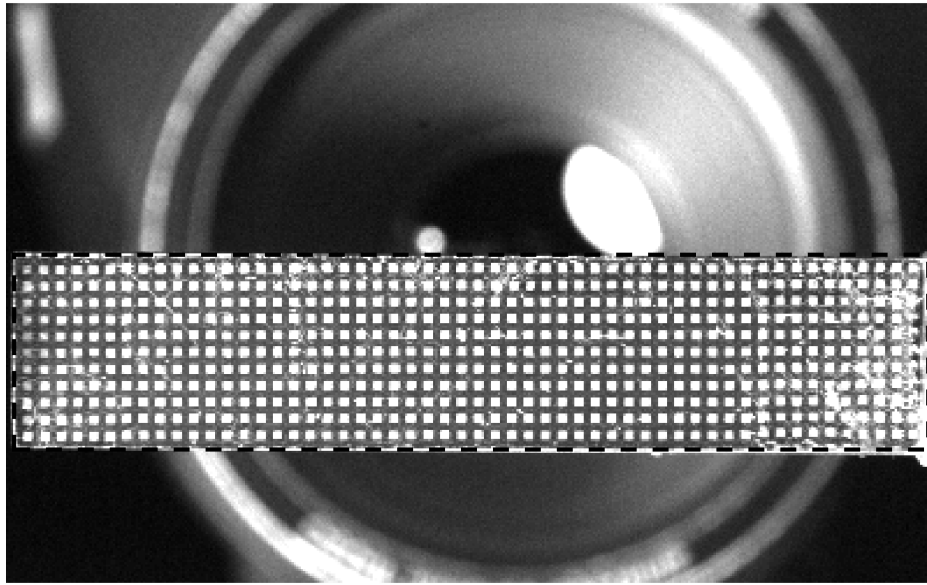
²noise equivalent differential temperature

³after double temporal differentiation

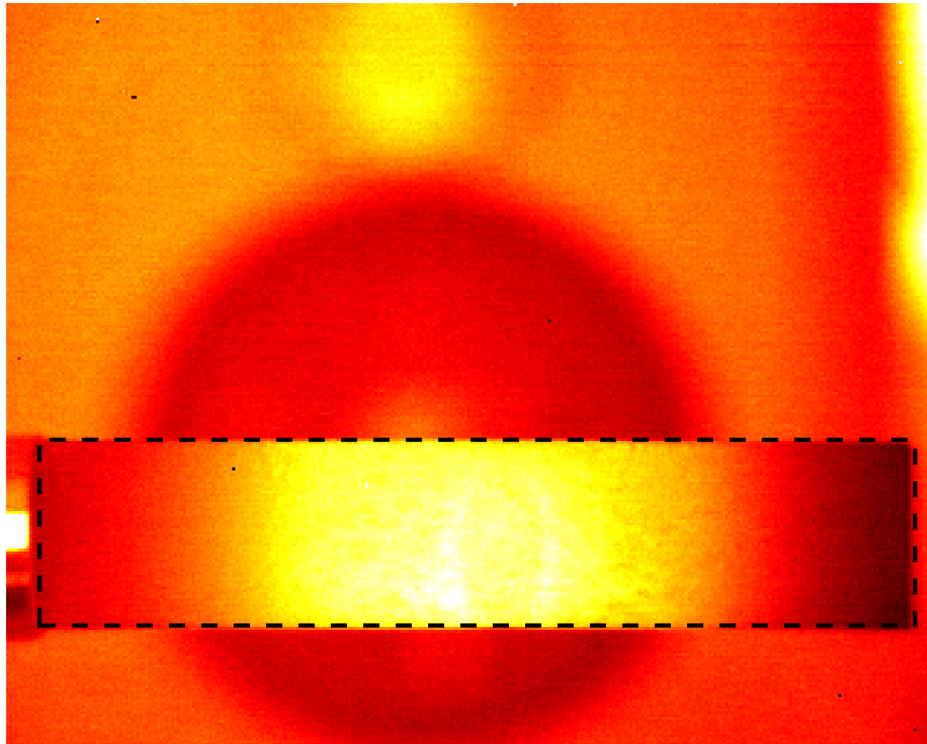
stationary images to be in the order of 3.5 % of pixel dynamic range. Details concerning the methodology used to obtain this value are provided in Section 2.3. The specimen was illuminated by a Gemini 1000Pro (1000 W) flash light from Bowens (UK). An example of a frame captured by the camera is shown in Figure 2a. The magnification was chosen to fit at best the sample length, the free edge is on the left part of the frame.

A bonded regular grid was used to extract the in-plane displacement fields through a phase-shifting algorithm [10]. The grid, from COLOURSENSE Ltd. (UK), was produced using the dry transfer technique, i.e. by outputting a vector artwork to a high resolution film negative and using a photo-lithographic technique to expose a carrier sheet coated with a photosensitive ink-based film deposited on top of a thin layer of glue. The resulting pressure-sensitive adhesive multi-layer was carefully aligned on the sample surface, manually pressed, and the carrier sheet simply peeled-off. The total thickness of the grid has been measured to be less than 100 μm , typically around 40 - 70 μm . It was demonstrated in [28] that an equivalently thick layer of epoxy glue did not disturb the strain measurements when compared to a strain gauge. The grid used in the present configuration had a pitch of 1 mm and was imaged through a 28 - 105 mm Nikkor lens, at a sampling of 7 pixels per period, allowing a field of view of 57×35 mm with a working distance of about 180 mm (see Figure 1).

A sample. The material chosen for this first investigation was a 4 mm thick, 55 mm long and 12 mm wide PMMA (Poly-Methyl-MethAcrylate) Acrycast[®] sample sourced from Amari Plastics Plc (UK). The sample length was chosen to ensure that its first longitudinal deformation mode was at 20 kHz. Quasi-static reference material properties were obtained at $\dot{\epsilon} = 10^{-2}$ in uni-axial stress configuration using a standard universal test machine. Back-to-back strain gauges were employed to take into account spurious bending. A tangent Young's modulus value of $E = 2.9^{\pm 0.1}$ GPa and a Poisson's ratio value of $\nu = 0.35^{\pm 0.01}$ were found. The material density was obtained by measurement of water displacement to a value of $\rho = 1160 \text{ kg.m}^{-3}$. In addition, the glass transition temperature T_g of the material has been measured using both DMTA and Differential Scanning Calorimetry (DSC), and found to be about $110^{\pm 5}$ °C. DMTA data has been obtained from a Q800 analyser from TA Instruments using the dual cantilever (bending) deformation mode at a loading amplitude and a frequency of 0.1 % and 1 Hz respectively and using a temperature ramp of $1 \text{ }^{\circ}\text{C.min}^{-1}$. In the present work, simultaneous deformation and IR temperature measurements are required. To achieve this, the sample was covered with a black matt paint on one face, to produce a uniform and high emissivity surface suitable for IR measurements and, on the other face, with the regular grid described above (see Figure 1).



(a) Example of an image of the sample at rest, from the UHS camera. The grid pitch is 1 mm. The lens of the IR camera can be seen in the background.



(b) Example of a temperature field captured during an ultrasonic run. The temperature rises due to the self-heating process can be seen at the centre of the sample while the sample left and right edges remain close to room temperature. The lens of the UHS camera can be seen in the background.

Fig. 2: Example of grabbed images. Sample dimensions are 52 mm \times 12 mm, with a thickness of 4 mm.

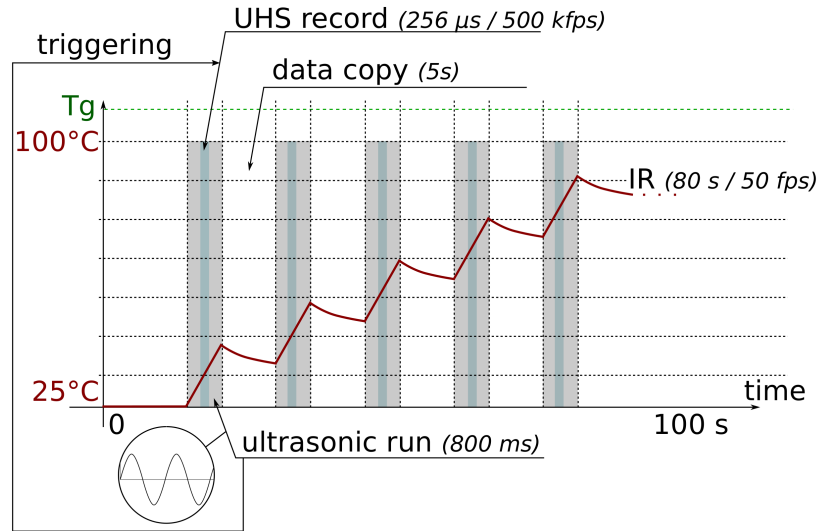


Fig. 3: Principle of the test.

2.2 Experimental procedure and data processing

The experiment consisted in a set of successive short ultrasonic runs during which both IR and UHS images were recorded. A schematic representation of the procedure is provided in Figure 3. The ultrasonic generator was programmed to produce, every 15 s, a 800 ms amplitude controlled cyclic loading and to send a trigger to the UHS camera. The flash light was triggered by the camera and a 256 μs image sequence of the deforming sample was recorded. The camera buffer was then automatically emptied by transferring the images to the computer and then re-armed for the next run. This operation lasts about 5 s depending on the computer and the connection speed. In parallel, the IR data were continuously recorded to capture the entire thermal history over a certain number of ultrasonic runs and for different loading amplitude. Indeed, this procedure can be applied for different loading displacement amplitudes, to produce sets of tests covering different strain-rate, temperature and heat-rate values. In the present paper, the procedure presented in Figure 3 was performed twice on a single sample, first at low displacement amplitude ($\pm 15 \mu\text{m}$), then at higher amplitude ($\pm 25 \mu\text{m}$) in an attempt to cover more of the strain-rate/temperature space. The 2nd series of test was conducted until the material locally reached its glass transition temperature (see Figure 3). All these points will be discussed later on in the article.

To summarize, the data set consisted of sets of discrete grid images sequences and continuous recordings of the surface sample infrared radiation. A schematic representation of the entire data post-processing procedure is provided in appendix. As introduced above, displacements were obtained from grid images using the grid-method [10]. In practice, initial and current image phases, ϕ_x and ϕ_y , were calculated individually through a windowed discrete Fourier

transform (WDFT) algorithm using a triangular windowing of $2N-1$ size, N being the grid sampling (number of pixels per period). The displacements were then obtained from the spatial phase shifts between a reference (first captured frame) and the following images according to the following equation:

$$U_i(x, y, t) = \frac{p}{2\pi} \Delta \phi_i(x, y, t) , \text{ with } i = (x, y) \quad (1)$$

where U_i is the displacement field along the direction i , $\Delta \phi_i$ is the phase shift along the same direction and p is the grid pitch. Because of the $2N-1$ kernel for the WDFT algorithm, one grid pitch is systematically lost at edges. As the whole displacement field is required for the data processing, especially at the sample free edge, missing data points were reconstructed using cubic spline extrapolation. Displacement fields were smoothed using a Gaussian filter (in space and time) before calculating derivatives and the optimal smoothing kernel size has been found to be $7 \times 7 \times 7$ along the x , y and time directions. Information concerning the choice of the smoothing kernel size are provided in Section 4. The final post-processing operation on the displacement consisted in finding and subtracting the initial deformation state. The choice of the initial undeformed reference image needs to be commented on at this stage. Indeed, stationary images were recorded before the start of each series of tests. However, because of the heating up of the specimen, thermal strains build up with time and the use of the unloaded image as a reference means that the strain fields will contain both thermal and mechanical strains, while only the later are of interest here. To avoid this issue, the first image of each ultrasonic run has been used as a reference image. This however leads to another issue. Indeed, as presented in Figure 3, for each run the first captured frame does not necessarily correspond to the sample at rest (ie, $t = 0$ in the harmonic response). Therefore, displacement fields based on such a reference need to be corrected. The fact that the loading is harmonic means that the average displacement of any material point over a period should be null. Such an assumption allows the identification of an offset field, i.e. the point by point average of the displacement over 5 periods, which is then subtracted from the initially estimated displacement. Finally, the displacements were averaged along the sample width as the test is assumed to be 1D. Strain, strain-rate and acceleration fields are subsequently simply obtained through simple and double centred finite difference while derivatives at sample boundaries are obtained through left- and right-hand side finite difference respectively. It is worth noting that acceleration fields can also be obtained through analytic differentiation as follows:

$$\tilde{a}_i(x, t) = -\omega^2 U_i(x, t) \quad (2)$$

with $\omega = 2\pi f$ the angular frequency. The systematic comparison between analytic derivation (see Eq: 2) and acceleration obtained from finite differences will be discussed within Section 4.1, dedicated to FE simulations, but finite

differences only were used for experimental data-processing in Section 3. This point will be discussed later on.

Infrared (IR) data were post-processed following the so-called pixel-by-pixel calibration strategy [34]. Sets of 20 IR reference images at different uniform and stabilized temperatures, from 20 to 90 °C, were captured using an extended area blackbody from Infrared System Development Corp. (USA). The mean response of each pixel of the IR focal plane array (FPA) as a function of the blackbody temperature was then fitted using a 5th order polynomial function to build up a set of coefficients which fully characterise the relationship between the raw digital level and the effective temperature for each pixel and over the expected experimental temperature range. This calibration was then applied to the experimental measurements to convert the raw data into temperature fields. As kinematic measurements have been obtained over discrete 256 μ s periods while infrared data were continuously recorded at 50 fps, the next step consists in finding the single measured thermal field corresponding at best to each kinematic sequence. In the present work, the thermal field taken at time nearest to half the loading period was simply selected. The impact of this choice on the accuracy of the thermal measurement regarding the considered kinematic sequence is discussed in the next section (Section 2.3). Finally, the selected thermal fields were downsampled using spline interpolation to fit the kinematic measurements resolution, and then, averaged over the sample width.

The procedure for reconstruction of stress fields and material identification will be detailed further in Sections 2.4 and 3.2.

2.3 Measurement uncertainty

The sources of uncertainty on the kinematic measurement are multiple. They can arise from the intrinsic sensor noise, the method used to recover displacements, the test conditions etc. . . This uncertainty can be partly quantified by grabbing a set of stationary undeformed images and applying the phase shifting algorithm [10] to recover displacements, and post-process these displacements (see Section 2.2) to derive strains, strain-rates and accelerations. The resulting identified noise takes into account all these potential sources of error, at least in static conditions. Unfortunately, it does not include errors arising from a misalignment of the sample with respect to the camera reference system and lens distortions which can create some fictitious deformations. It also does not take into account lighting variations and grid defects. Therefore, it can be considered a lower bound of the deformation uncertainty. It should also be noted that the discretized deformation measurement acts as a low pass spatial filter. The systematic error generated by this is explored in Section 4.2.

Concerning the infrared measurements, the uncertainty is mainly driven by five parameters: (1) the intrinsic noise of the sensor under perfect conditions, *i.e.* the NEDT over the studied temperature range - (2) the accuracy of the calibration procedure - (3) the surface emissivity distribution and variations - (4) the setup environment and (5) the triggering mismatch. The impact of the environment and emissivity distribution has been mitigated by applying a high emissivity uniform coating to the sample and covering the entire setup with a black curtain during the whole test to avoid IR reflections from the surroundings. The thickness of the coating can also be a problem since it tends to delay the transmission of the thermal information from the specimen to the paint surface [31]. However, this has not been investigated here as the accuracy requirements for the temperature readings are not as stringent as for thermal stress analysis as used in [31]. As detailed in Section 2.2, the calibration was performed using a pixel-by-pixel calibration to minimize the uncertainty. The last point is not exactly a problem of temperature uncertainty but relates to the synchronization of the kinematic and thermal data. Indeed, the temperature was recorded at a lower frame-rate than the kinematic data, and no synchronization between the UHS and IR cameras had been implemented. One can decompose this uncertainty as the sum of: (1) the unknown temperature variation during the few cycles captured by the UHS camera - less than 5 mK - (2) the temperature variation between 2 IR images - about 500 mK - and (3) the unknown concerning the precise time when the UHS frames were grabbed with respect to the IR timeline - less than 5°C. The value provided depends on the material self-heating rate and is therefore only valid for the experimental conditions described above (see Section 2.2). It is worth noticing that the last point is not an intrinsic problem of the method and will be solved in further experiments. However, it is important to keep in mind that the 5°C uncertainty in the present case is acceptable as the material temperature sensitivity remains low over this temperature range.

Table 1 summarizes the experimental parameters and reports the related uncertainties. These were calculated from a set of 128 images of the stationary specimen recorded in the same conditions as that of the test just before the start of the ultrasonic horn.

- The grey level noise was obtained by calculating the standard deviation over time at each pixel, and dividing it by the mean grey level value at that pixel. This was then averaged across all grey level values. The sensor noise variation as a function of the sensor dynamic range is discussed in Section 4.2.
- The strain, strain-rate and acceleration noise values were obtained from the standard deviation in space and time of the average value across y (as the strain will be obtained for the stress-strain curves).
- The stress noise was calculated from the acceleration noise by averaging over the length and multiplying by the density, as in Eq. 3.

Sample ($\dot{\epsilon}=10^{-2}$)	Material	PMMA
	Dimensions (mm)	55 x 12 x 4
	Density ($\text{kg}\cdot\text{m}^{-3}$)	1160
	Young's modulus (GPa)	$2.9^{\pm 0.1}$
	Poisson's ratio	$0.35^{\pm 0.01}$
	T_g ($^{\circ}\text{C}$)	$110^{\pm 5}$
Grid	Thickness (μm)	<100
	Grid pitch (mm)	1
	Sampling ($\text{pixel}\cdot\text{period}^{-1}$)	7
IR	Model	CEDIP Silver 480M
	Lens	27 mm
	Frame rate (fps)	50
	Integration time (μs)	509
	Number of pixel (pixel^2)	320×256
	Field of view (mm^2)	60×48
	Uncertainty	< 5 $^{\circ}\text{C}$
UHS	Model	Shimadzu HPV-X
	Digitization	10 - bit
	Lens	28 - 105 mm Nikkor
	Frame rate (kfps)	500
	Number of pixel (pixel^2)	400×250
	Max. sensor noise (% of grey levels)	3.5
	Field of view (mm^2)	57×35
	Smoothing window (x,y,t)	$7 \times 7 \times 7$
	Displacement noise	$0.6 \mu\text{m}$ or 5×10^{-3} pix
	Strain noise (Finite diff. in μdef)	± 195
	Strain-rate noise (Finite diff. in s^{-1})	± 25
Acceleration noise (Finite diff. in $\text{m}\cdot\text{s}^{-2}$)	$\pm 1.3 \times 10^4$	
Stress noise (MPa)	± 0.15	

Table 1: Experimental parameters and uncertainties obtained from stationary images.

2.4 Theoretical framework

This section describes how acceleration maps can be used to derive stress information using a simplified version of the dynamic equilibrium equation. The extent of possible loading ranges accessible with such a setup is then explored.

2.4.1 Acceleration as a load-cell

As already shown in [27,25], it is possible to reconstruct average stress distributions along the length of the sample from the following relationship (obtained from basic dynamic equilibrium considerations):

$$\overline{\sigma_{xx}}(x,t) = -\rho x \overline{a_x}(x,t) \quad (3)$$

where $\overline{\sigma_{xx}}(x,t)$ is the average Cauchy stress over the transverse section coordinate y , ρ is the material density, and $\overline{a_x}(x,t)$ is the surface average of the longitudinal acceleration component between the free edge, and the considered

section of coordinate x (see Figure 4). Such an equation relies on two main assumptions: the homogeneity of the acceleration through the thickness and the homogeneity of the material density over the whole sample. For the latter however, it is possible to update the density using the strain information [15]. Since strains are also obtained by spatial differentiation of the displacements, an assumption of uniaxial loading means that stress-strain curves can be directly reconstructed in many sections of the sample which see different strain, strain-rate and temperature levels.

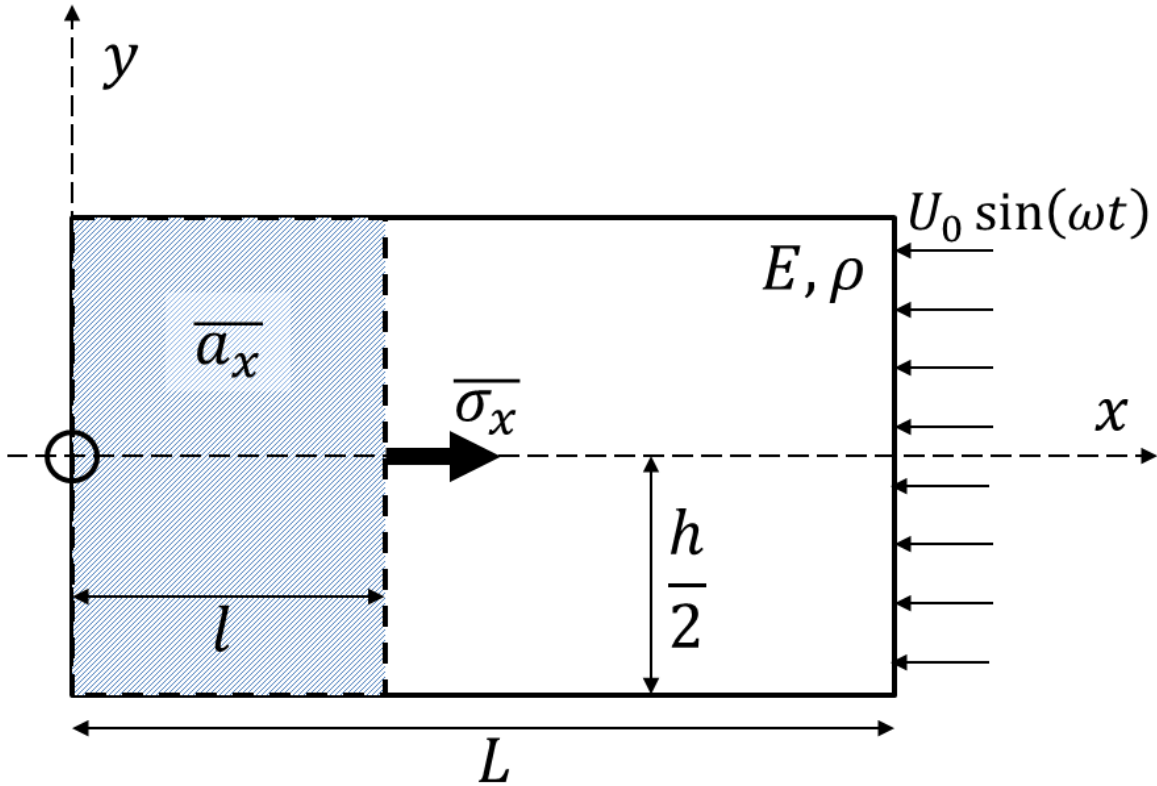


Fig. 4: Schematic of a sample subjected to longitudinal inertial loading.

One understands here that the stress reconstruction precision will depend on three main elements: (1) the accuracy of the material density value which plays the role of load cell factor here, (2) the temporal resolution of the grey level images which will affect the acceleration and (3) the spatial resolution as Eq. 3 stems from discrete approximations of spatial integrals [25,27]. In practice, an additional issue arises from the fact that strains are obtained on average over a grid pitch and expressed in its centre, while stresses are obtained on a slice. An additional step consisting in interpolating the stress values at grid centroids will be required to produce consistent stress-strain curves and identified material properties.

2.4.2 High-power ultrasonic excitation

One of the key elements of the present methodology is the ability to produce a heterogenous thermo-dynamical state within the material. Such state could be achieved using different strategies, for instance playing on the sample geometry and/or on the loading itself. The choice here is to develop longitudinal stationary waves within the sample. The frequency, the wavelength and the amplitude of such deformation waves will drive the characteristics of the loading.

Let us assume that the displacement field within the sample can be described as the product of a spatial and temporal sine function such as:

$$u(x,t) = u_0 \cos(\omega^s x - \Phi^s) \cos(\omega^f t - \Phi^f) \quad (4)$$

where:

- u_0 is the amplitude of loading
- $\omega^s = \frac{2\pi}{L_n}$ is related to the spatial deformation wave, with $L_n \approx \frac{1}{f} \sqrt{\frac{E}{\rho}}$ the deformation wavelength (f the loading frequency) and $\sqrt{\frac{E}{\rho}}$ the speed of sound in the material;
- $\omega^f = 2\pi f$ is the angular frequency, with f the loading frequency;
- Φ^s and Φ^f are the spatial and temporal phases.

With this description, it is possible to evaluate the levels of maximum strain, strain-rate and acceleration that can be achieved with the current setup:

$$|\epsilon_x^{max}| = \left(\frac{\rho}{E}\right)^{\frac{1}{2}} u_0 \omega_f \quad (5)$$

$$|\dot{\epsilon}_x^{max}| = \left(\frac{\rho}{E}\right)^{\frac{1}{2}} u_0 \omega_f^2 \quad (6)$$

$$|a_x^{max}| = u_0 \omega_f^2 \quad (7)$$

Three main parameters drive the deformation amplitude: the amplitude of the displacement and the loading frequency, both imposed by the actuator, and the deformation wavelength arising from the material itself.

As a consequence, reaching a strain-rate of *e.g.* 200 s^{-1} at a frequency of 20 kHz (standard frequency for high power ultrasonics) requires a peak-to-peak amplitude of $20 \text{ }\mu\text{m}$ for a PMMA sample ($\rho = 1200 \text{ kg.m}^{-3}$, $E = 3 \text{ GPa}$). In other words, covering a large strain-rate domain requires high-power ultrasonics, *i.e.* both high amplitude and high frequency. This is generally opposed to low-power ultrasound (hundreds of nanometers) which are used for diagnostics and control and does not significantly affect the environment in which the wave propagates. Keeping the

values given above, the associated strain amplitude would be of the order of $\pm 0.2\%$, without taking into account any thermal effects, and the acceleration would reach 320 km.s^{-2} , i.e. $> 3 \times 10^4 g$. Spatially, if the sample is designed to be resonant at its first longitudinal mode, *i.e.* the sample length is half the wavelength, the sample undergoes high displacement and zero strain on free and fixed edges (see Figure 4) and high strain and strain-rate at its centre. In addition, due to the viscoelastic dissipation, the central part of the sample will heat up cycle after cycle, while the edges will remain almost at room temperature. The last point is due to the significant mismatch between the characteristic conduction time within a PMMA sample [12] and the loading frequency, providing adiabatic conditions during loading.

The above shows that it is possible to reach large strain-rates in the material, of the order of hundreds of s^{-1} , with a heterogeneous state of strain, strain-rate and temperature which enables to test the material over a wide range of thermo-mechanical conditions within a single test. The present article aims at demonstrating the experimental feasibility of this idea and at providing initial results on PMMA.

3 Results and discussion

3.1 Presentation of the results

A single PMMA sample was submitted to the experimental procedure detailed above (see Section 2.2). Successive sequences of grey level images were captured while the temperature was continuously recorded until the sample reached its glass transition temperature. The test was composed of two series of successive ultrasonics runs. In the first series, six ultrasonic runs were successively applied to the sample at low power, leading to a maximum strain of $\pm 735 \mu\text{def}$. It was then followed by five other runs at a higher actuator power, leading to a maximum strain of $\pm 1542 \mu\text{def}$. Between both test series, the sample was allowed to cool down back to room temperature.

Figure 5 presents the temperature record at the highest power (2^{nd} series). The red lines show the different instants when short ultrasonic runs were applied (shaded region in Figure 3) and the map shows how the sample temperature profile (averaged over the sample width) evolves as a function of time. During each loading (800 ms), the sample rapidly heated up (within the red line) and then cooled down until the next run. Figure 5 shows this cooling process with a slight decrease in temperature between two red lines. Only 4 s before and after each ultrasonic loading are shown on the figure. Black dots symbolize the skipped IR frames.

Figure 6 shows the evolution of the measured longitudinal displacement, strain, strain-rate and reconstructed stress profiles as a function of time. The data corresponds to the first ultrasonic run at higher strain amplitude (2^{nd} series),

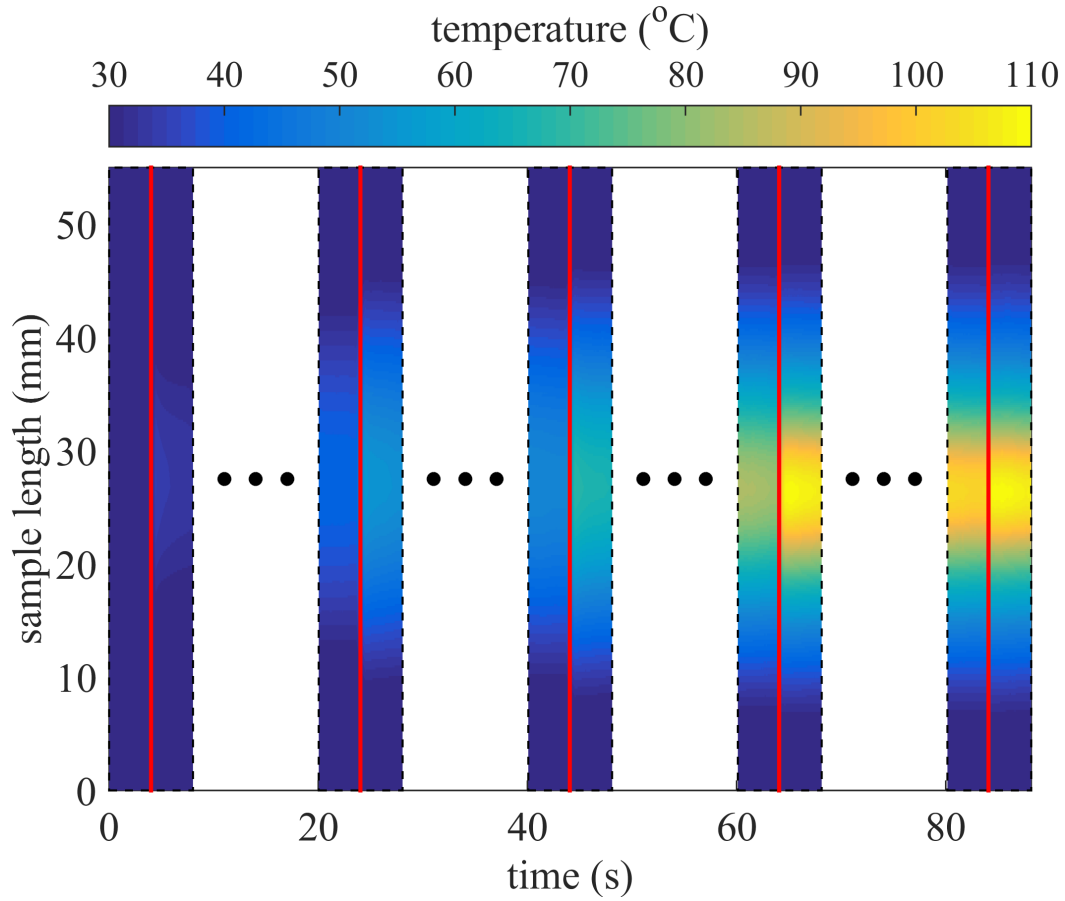


Fig. 5: Temperature profiles (along sample length) as a function of time during the second ultrasonic test series. Red lines are loading instants while the black dots are used to symbolize the delay between loading instants.

i.e. within the first red line in Figure 5. As stated in Section 2, the data at a given time step is represented as a 1D signal, therefore, Figure 6 shows space vs time plots. These maps evidence that the sample is indeed loaded on its first longitudinal deformation mode, since stationary and half wavelength waves can be observed during the 256 μs captured by the camera. The sample undergoes a cyclic displacement of $\pm 25 \mu\text{m}$, cyclic deformation of $\pm 1500 \mu\text{def}$, cyclic strain-rate of about $\pm 200 \text{s}^{-1}$ and a cyclic stress of about $\pm 7 \text{MPa}$. Regarding Figure 5, the sample undergoes also a local increase of temperature up to 110 $^{\circ}\text{C}$ at the end of the test while the sample edges remains close to room temperature. The following thermo-mechanical fields are consistent with the analytic estimates presented in Section 2.4.2 and confirm the heterogeneity of the thermodynamical state within the material.

Going down into the detail of each ultrasonic run, Figure 7 presents the strain, strain-rate and stress amplitude profiles (half peak-to-peak) as well as the temperature profiles for every successive ultrasonic loading. Such profiles are computed by calculating, for each sample section, half of the peak-to-peak amplitude over 5 ultrasonic cycles

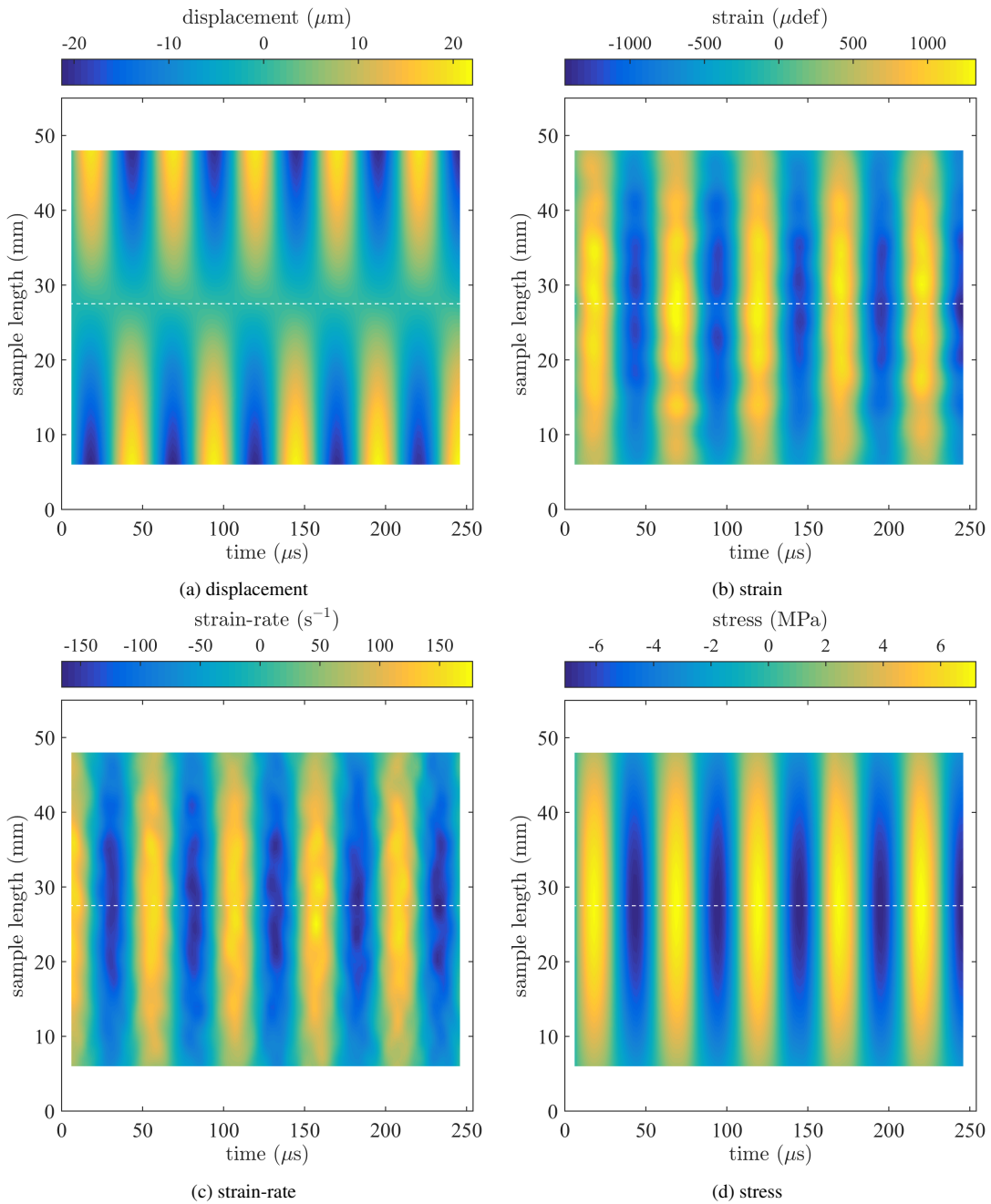


Fig. 6: Displacement, strain, strain-rate and stress as a function of time. The data have been averaged across the specimen width. The data corresponds to the 1st vertical red line in Figure 5.

(see Figure 6) for each of the 11 successive ultrasonic runs. Apart from visualisation, the following data is used to define the value of the apparent strain-rate per sample section. Indeed, each section undergoes a cyclic load and thus, a range of strain-rates. Nevertheless, as it is usually assumed in standard Dynamic and Mechanical Analysis,

for a sake of simplicity, the time variation can be collapsed into a single apparent strain-rate value defined here as half the amplitude of strain-rate seen by each section. The consequences of this assumption are discussed further in Section 5. Finally, the frame-rate of the IR camera does not allow a temporal description of the temperature field over each cycle. As a consequence, each temperature profile presented in Figure 7d only results from a single frame. The strain and strain-rate data close to the free and fixed edges have been discarded because of edge artefacts from the Gaussian smoothing of the displacement fields. It is also important to note that the temperatures over 90 °C (see dashed rectangle in Figure 7d) have been reconstructed using cubic spline interpolation. Indeed, due to the chosen integration time, the camera sensor saturated above 90 °C. An integration time of about 400 μ s or a multi-IT strategy would have been more suitable to capture the range [25 - 110] °C.

One observes that, when the sample is loaded at $\pm 735 \mu\text{def}$ (1st series), the strain amplitude varies continuously along the sample length from 400 to 735 μdef , the strain-rate amplitude from 50 to 115 s^{-1} , the stress amplitude from 0.2 to 4 MPa, and the temperature slightly increases in the sample centre from 23.3 to 34.6 °C while the edges remains at room temperature.

When the sample is loaded at $\pm 1542 \mu\text{def}$ (2nd series), the strain amplitude varies from 200 to 1542 μdef , the strain-rate amplitude from 40 to 220 s^{-1} , the stress amplitude from 0.2 to 7.6 MPa, and the temperature increases in the sample centre from 23.4 to 105 °C. Contrary to the first test series where all curves overlapped almost perfectly, the second series evidences a softening of the material as demonstrated on Figure 7c. This is due to significant increase of the temperature cycle after cycle (see 7d). A clear change of the material response can be observed at the 4th and 5th ultrasonic runs. These two loading cases are characterized by a significant drop of the stress down to 6 then 3 MPa as well as clear change in the profile shapes. Indeed, one can see on Figure 7a a clear strain localization in the sample centre and a significant decrease of the strain level everywhere else. These phenomena are due to a sharp localized change in the stiffness of PMMA due to glass transition. The phenomenon starts at the 4th run, i.e. around 95 °C but leads a clear collapse of the material stiffness at the 5th run, i.e. around 105 °C. Such a drastic local change in material property also leads to a significant change in the deformation mode of the sample. Indeed, while the material is initially perfectly tuned to be resonant on its first longitudinal mode at 20 kHz, one observes a significant decrease of the wavelength (see Figure 7c) at the 4th and 5th runs. This point is the reason why finite differences have been used to obtain experimental acceleration fields as the assumption of homogeneous material response cannot be ensured anymore. According to the wavelength formulation, available in Section 2.4, a decrease of the wavelength relates to a drop of the stiffness which will be evidenced further. In the present case, the temporal resolution (50 Hz) of the temperature signal combined with the heating rate does not allow finely capturing the T_g , but a value around 100 °C is

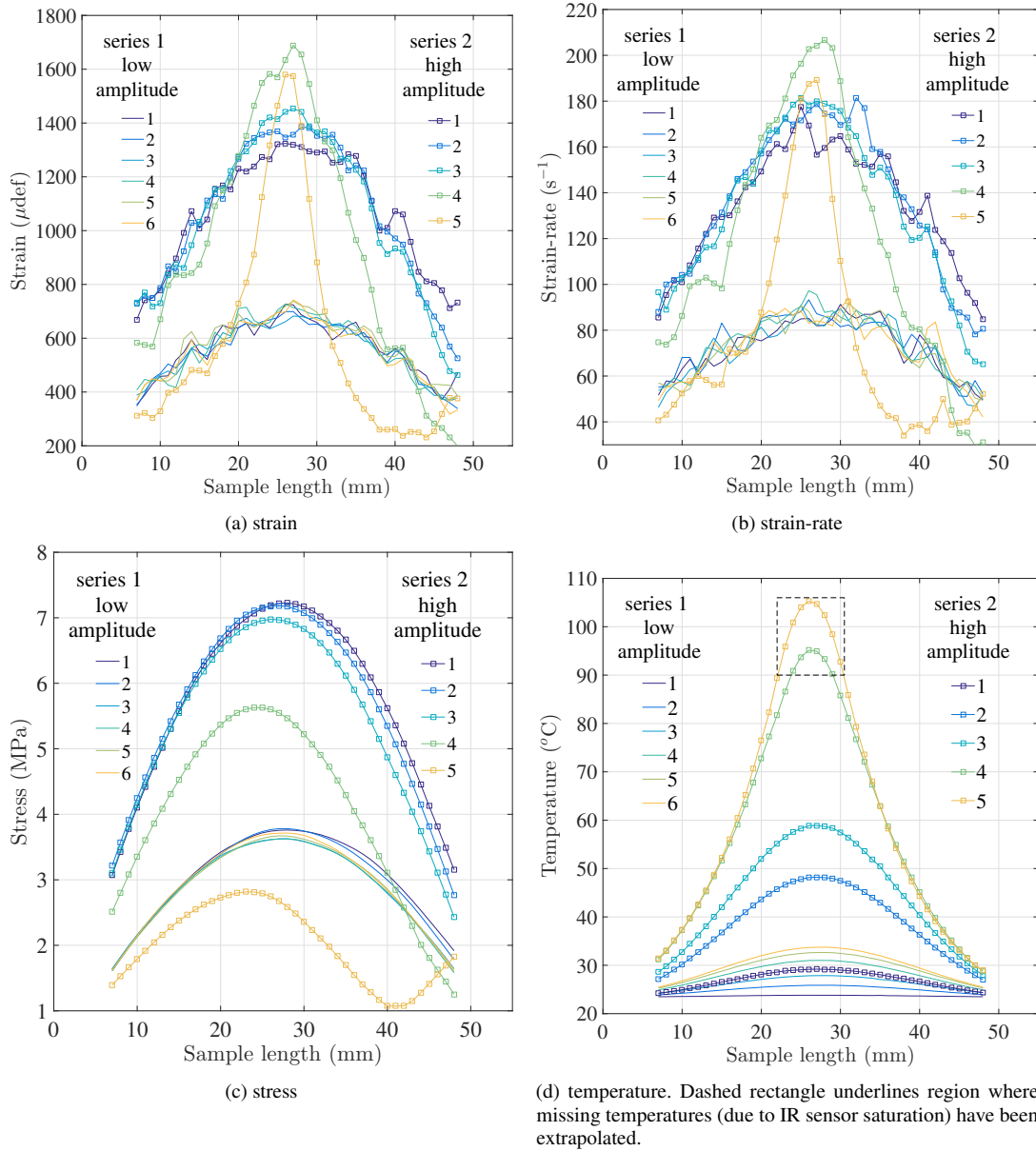


Fig. 7: Strain, strain-rate, stress and temperature profiles (along sample length) for each ultrasonic run. The free edge is at 0 mm while the fixed edge is at 55 mm.

reasonably in line with glass transition temperatures measured on the material using DMTA (see 1).

The data can now be combined to identify the material properties as a function of temperature and strain-rate.

3.2 Storage modulus and damping identification

Figure 8 presents the evolution of the material response within three different sample cross-sections (at $\varepsilon = \pm 1542 \mu\text{def}$, i.e. test series 2 - cf. Figure 7) and for different ultrasonic runs. The dots represent the experimental data while the curves are based on a sinusoidal least-square fit. Both stress and strain are temporally fitted by a sine function as follows:

$$\varepsilon_f(x, t) = \alpha_0 \sin(2\pi ft + \phi_0) \quad (8)$$

$$\sigma_f(x, t) = \alpha_1 \sin(2\pi ft + \phi_1) \quad (9)$$

where f is the loading frequency, t is the time, x is the axial position and α_i and ϕ_i are the amplitudes and phases of strain and stress for $i=0$ and $i=1$ respectively. From this description, $\tan(\delta)$ can also be obtained from the temporal phase shift between the stress and the strain as follows:

$$\tan(\delta)(s, t) = \tan(\phi_0 - \phi_1) \quad (10)$$

This parameter is widely used to describe the damping of the material. The real part of Young's modulus, the storage modulus, is then identified from the ratio $\frac{\alpha_1}{\alpha_0} \cos(\delta)$.

The results show a number of important trends. Looking at Figure 8a of the first run when the temperature in the specimen is still uniform (see Figure 7d), one can see that the central sections provide a stiffer response than the outward one. This is the stiffening effect of strain-rate. Based on the data in Figure 7b, the material at 10 mm experiences a strain-rate of about 50 s^{-1} while the centre responds under a strain-rate of about 80 s^{-1} . Both stiffness and strain-rate contrasts are not very large but the effect is significant. The second trend is the effect of temperature, which is much more prominent for this test. As the runs progress and the temperature increases at the centre of the sample, the stiffness drops as clearly seen in Figure 8c and consistently over the whole test series. Finally, it is also clear from Figures 8 that as the temperature increases, the hysteresis loops open up, indicating an increase in damping.

Based on the following local stress-strain relationships, the storage modulus and $\tan(\delta)$ have been identified and the results are presented in Figure 9. Figure 9a presents the variation of storage modulus as a function of strain-rate and temperature. The red dots are the experimental data points obtained by combining information over 42 material sections (55 lines minus two filtering kernels to discard edges artefacts) and eleven ultrasonic runs, i.e. 462 data points. It is important to understand that each material slice is treated independently of its neighbours as if this was a separate material test. The continuous colour map is obtained by interpolating the data between the red dots using the Matlab[®]

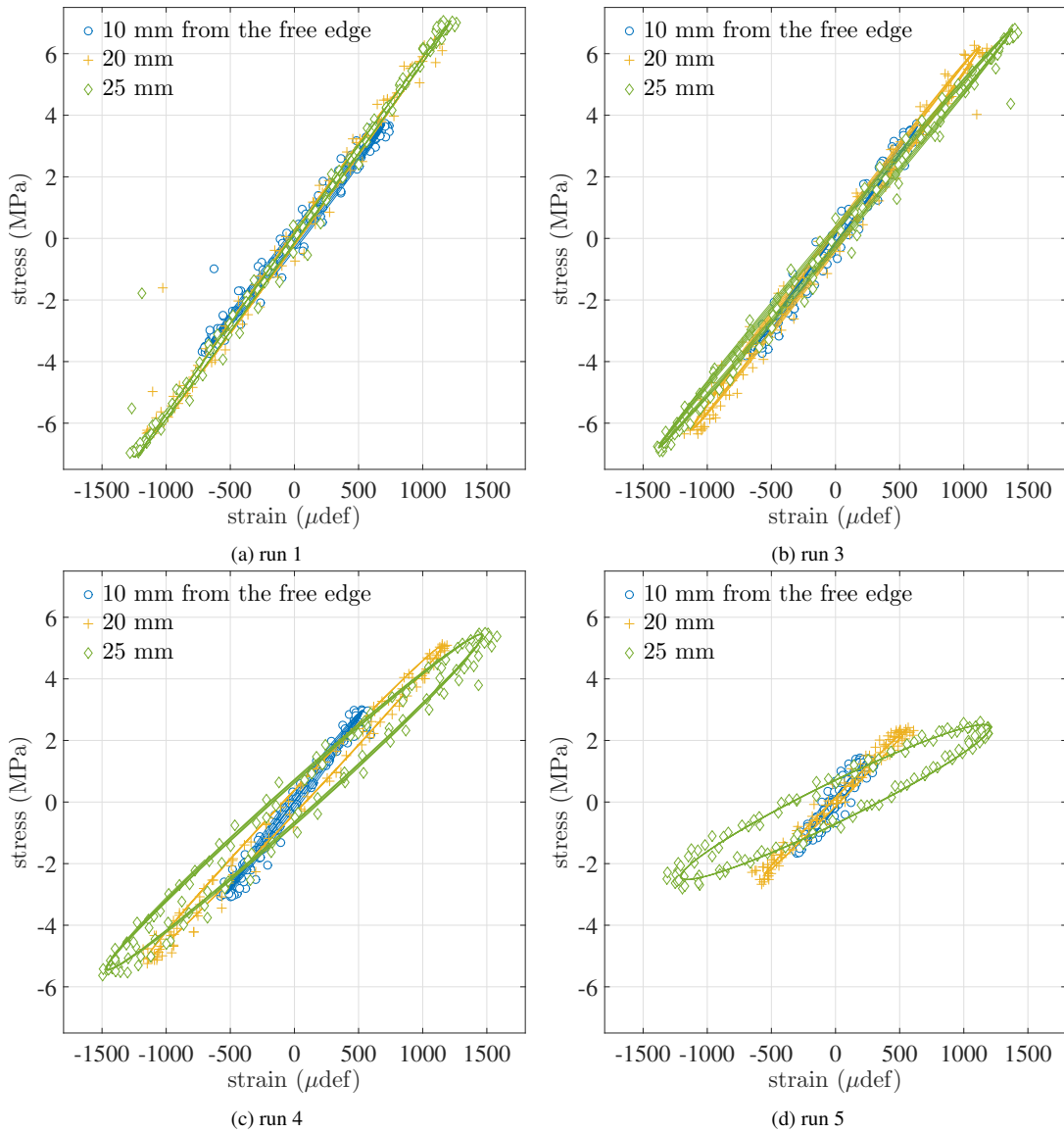


Fig. 8: Stress-strain curves for 3 different sample sections, from free edge to sample centre, and for different ultrasonic runs during the 2nd test series, i.e. high strain-rate amplitude.

embedded natural neighbour interpolation method based on Voronoi tessellation. The figure shows the range of the current experiment, i.e. strain-rates between 30 and 220 s⁻¹ and temperatures between about 25 and 105 °C. Within this 2D loading condition space, the storage modulus varies from 1.5 GPa, at high temperature, up to 6.3 GPa at low temperature. The experiment clearly captures the temperature sensitivity of PMMA with a strong vertical gradient in the map in Figure 9a. Looking at the isothermal curves (horizontal gradient), a slight strain-rate sensitivity can also be noticed, as expected. This effect is small however as the strain-rate range covered here is rather small. One can also observe higher noise on the data for the lower strain-rate and temperature ranges. This corresponds to sections

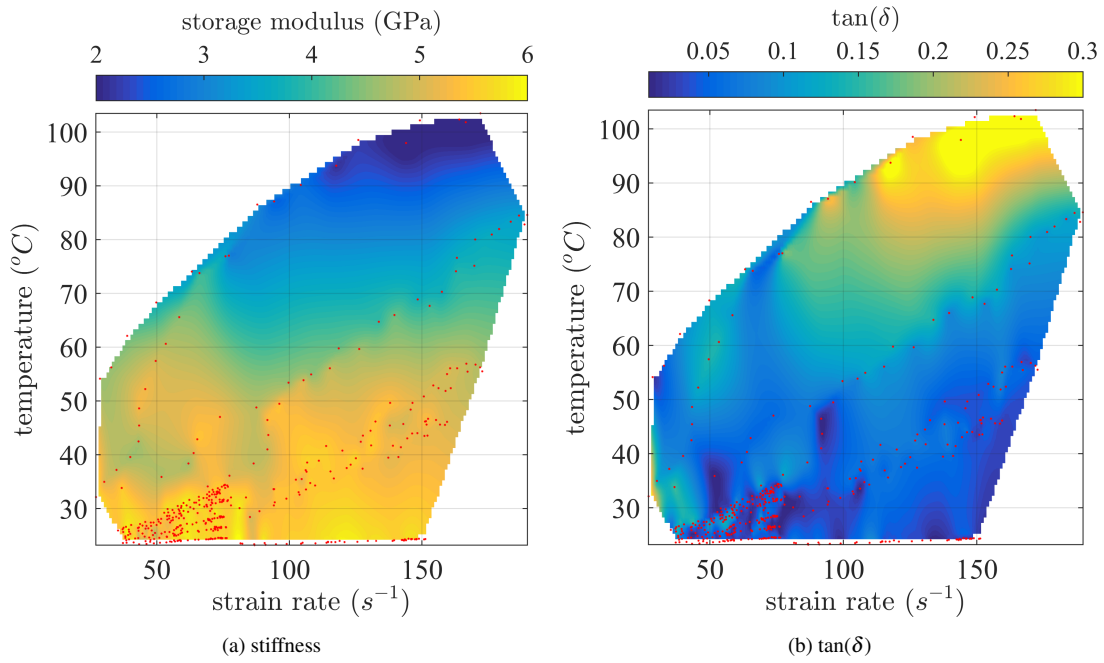


Fig. 9: Identification of storage modulus and $\tan(\delta)$ as a function of strain-rate and temperature.

close to the specimen edges where both stress and strain are lower and therefore, exhibit degraded signal to noise ratios.

Then, Figure 9b presents the variation of the $\tan(\delta)$ parameter which is associated to the material damping. A few excessively high and unrealistic damping values have been discarded (less than 10 data points higher than 0.4) and the colormap saturates at 0.3 to visually capture the local gradients. The same trend as for the storage modulus is observed, although the data are noisier. This was expected as $\tan(\delta)$ derives from small fractions of the total stress and strain. As for the storage modulus, the noise is larger in the low temperature and low strain-rate range, for the same reason. It is interesting to compare these data to that available in the literature. Looking for instance at [18], the variation of $\tan(\delta)$, from ambient to 105 °C, ranges between about 0.03 and 0.3 which is the range also observed here. Another interesting observation is that there is a trend for higher values at low strain-rate and temperature. This may be related to the presence of a β -transition around room temperature, but the poor signal to noise ratio there precludes any definite conclusion. More tests are needed to explore this part of the temperature / strain-rate space.

From a technical point of view, both graphs evidence a very heterogeneous data-point density. Indeed, Figure 9a has a large significant data-point density between 50 and 100 s^{-1} for temperature comprised between ambient and 35 °C whereas very few data-points are available at higher temperature. This point is not intrinsic to the method and mainly depends on the chosen ultrasonic loading amplitudes. In the present work, only two amplitude steps have been

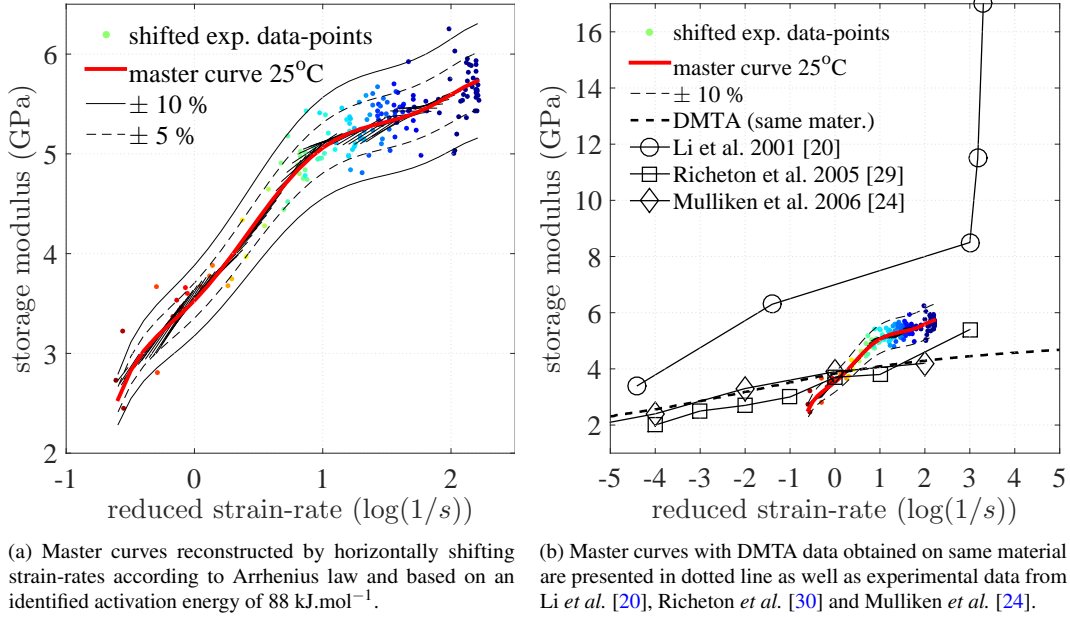


Fig. 10: Master curves at 25°C on PMMA.

used ($\pm 735 \mu\text{def}$ and $\pm 1542 \mu\text{def}$). Using more steps would have led to a more homogeneous space sampling.

Finally, time temperature superposition has been used in an attempt to collapse all the data in Figure 9a on a single master curve. To achieve this, experimental data points undergoing low strain-rates ($< 70 \text{ s}^{-1}$, see Section 4 for details), and the ones close to T_g and post T_g have been discarded. For the latter, as the glass transition was not identified accurately, the procedure has consisted in removing data over a threshold damping value of 0.3 (see top yellow region in Figure 9b) and a threshold temperature value of 95°C .

For thermo-rheologically simple materials, *i.e.* materials that obey time-temperature superposition which is the case of PMMA below the T_g , it is assumed that an increase in temperature is equivalent to a decrease in strain-rate. The reconstruction of a master curve consists therefore in shifting isothermal storage modulus curves along the strain-rate axis by a factor a_T until a single curve is obtained, representing the evolution of the material behaviour at a fixed reference temperature T . The shifting factor a_T can be described by the Arrhenius equation as follows:

$$a_T(T) = \exp\left(\frac{\Delta H}{R} \left(\frac{1}{T} - \frac{1}{T_0}\right)\right) \quad (11)$$

where ΔH is the activation energy associated with mechanisms of internal friction, $R = 8.3144598 \text{ J}\cdot\text{mol}^{-1}\cdot\text{K}^{-1}$ is the gas constant, and T_0 is a chosen reference temperature. Figure 10a shows the identified master curve at 25°C . Storage modulus values are presented with scattered points (from blue (ambient) to red (hot)). Individual slopes

of storage modulus isothermal curves are presented with multiple straight black lines and the master curve and its $\pm 5\%$ and $\pm 10\%$ vertical shifts are presented with plain and dotted lines respectively. In practice, to obtain such a master curve, storage modulus isothermal curves (horizontal slices in Figure 9a) were first individually fitted by affine functions in order to obtain a first order description of their slopes. Such set of approximated isothermal curves can be seen in Figure 10a all along the master curve. Then, a 6th order polynomial function was used to fit the whole set of approximated isotherms as a function of the reduced strain-rate. Finally, a sweep on the activation energy value, thus on the shifting factor (see Eq. 11), was performed and the difference between the isotherms and the polynomial approximation calculated. An identified activation energy of $88 \text{ kJ}\cdot\text{mol}^{-1}$ has been found to minimize this deviation in the least-squares sense. The identified activation energy is in same order of magnitude than values found in the literature, see *e.g.* [1] where an activation energy of $71 \text{ kJ}\cdot\text{mol}^{-1}$ has been found for PMMA samples tested with a Broadband Viscoelasticity Spectrometer (BVS), or $90 \text{ kJ}\cdot\text{mol}^{-1}$ in [11]. In addition, it is worth mentioning that the scatter of the storage modulus falls within a $\pm 10\%$ error band around the master curve, with a decrease of the scatter down to $\pm 5\%$ at higher temperatures, and that the isotherms follow reasonably well the trend over 2 decades of strain-rate. Such a comparison demonstrates the relevance of the data extracted from the current ultrasonic experiment.

The reconstructed master curve at 25°C is also presented in Figure 10b with a set of data from the literature. In addition, DMTA was performed on the same material using a Q800 system from TA Instruments. A stepwise temperature control with a 1°C interval between each step was used during the measurements. The testing temperature ranged from -80°C up to 50°C and the data were recorded at multiple frequencies: 0.1, 0.3, 1, 3, 10 and 30 Hz. The $17.25 \times 12.07 \times 3 \text{ mm}^3$ specimen was subjected to a dual cantilever deformation mode⁴ and the strain amplitude was kept lower than 0.1%. Comparing the present "one-shot" material characterisation to DMTA and literature results, a certain discrepancy can be observed (see Figure 10b). The present results are located between that from [20], where the material was subjected to compressive tests at quasi-static (servo-hydraulic machines) and high strain-rates (SHPB), and [24, 30] with data from DMTA and compressive tests on both servo-hydraulic machines and SHPB. The trends are similar but the current data lie about 1 GPa above that from [24, 30], while they are about 2 GPa below that in [20]. An interesting thing is the fact that the data in [30] and [20] as well as the current data (partially) evidence an inflection in the behaviour somewhere between 10^1 and 10^3 s^{-1} , which is not visible on both DMTA result. Nevertheless, more experiments, at higher strain-rates, or at lower temperatures (through the time-temperature superposition principle) are necessary to confirm the existence of such a sharp increase of the material stiffness at high strain-rate as well as the ability of high-speed tests, contrary to standard DMA, to capture it.

⁴similar to 3-point bending except that ends of the sample are clamped

The focus of the present work is not to perform a thorough study of the viscoelasticity of PMMA but to propose a truly new test method to reach strain-rates that are generally hard to obtain as they lie between what can be obtained with high speed hydraulic machines on one side and split Hopkinson bars on the other side. The data in Figure 10b shows the benefit of having an alternative to the current test techniques to better explore the behaviour of viscoelastic materials at high rates of strain directly, without having to rely on time-temperature superposition, as for DMTA tests. The lack of transition at high strain on the DMTA data is a hint that this test may be missing some important transition. The difficulties associated with tests on high speed hydraulic machines and SHPB contrast with the relative simplicity of the current configuration and the present authors strongly believe that this new test can be a valuable addition to the toolkit of the mechanics of materials researchers and engineers.

The objective of the last section is to shed some light on the issue of the low spatial resolution of the camera. Indeed, the digitized measurements provided by the camera and the grid method are a spatially filtered version of reality and the only way to understand the effect of this filter on the quality of the identification is through numerical simulation.

4 Finite element validation

The purpose of this section is to validate the current experimental choices by understanding how experimental parameters such as the camera spatial resolution, the acquisition frequency, the grid sampling, the camera sensor noise and the sensitivity of the algorithm used to recover deformations can affect the precision of the identification. The idea is also to propose some guidelines to the reader and make this new technique more accessible. The main concern is the poor camera spatial resolution (400×250 pixels) so this validation is essential to give confidence to the previous results.

4.1 Finite element model

The Finite Element (FE) simulation consisted in an 3D harmonic analysis achieved using the ANSYS 16.2 FE package. Thanks to the problem symmetry, only a quarter of the sample was modelled. The model was meshed using 0.1 mm^3 *SOLID186* quadratic elements and a harmonic loading of amplitude $30 \mu\text{m}$ was applied to the right-hand side edge of the model (see Figure 11).

The material was modelled using an isotropic, homogeneous and purely elastic material. In other words, the present FE investigation does not deal with the impact of material time-dependence, *i.e.* impact of temperature and strain-rate variations along the sample length, nor the dissipation, on the identification validation process. This was

found reasonable as a first step to quantify the effect of the camera spatial resolution on the measured and identified quantities. The main characteristics of the FE model are summarized in Table 2.

Geometry	dimensions (mm)	55 x 6 (sym.) x 2 (sym.)
Mesh	size (mm ³)	0.1
	element	<i>SOLID186</i>
Material	density (kg.m ⁻³)	1160
	Young's modulus (GPa)	5.5
	Poisson's ratio	0.34
Loading	type	disp.
	amplitude (μm)	30
	frequency (kHz)	20
Analysis	FE package	ANSYS 16.2
	type	harmonic / full
	solver	Jacobi Conjugate Gradient iterative equation solver
	num. damping (s)	$\times 10^{-7}$

Table 2: FE model parameters

Figure 11 shows an example of an FE longitudinal displacement field extracted at the top surface of the model and then symmetrized along the transversal direction.

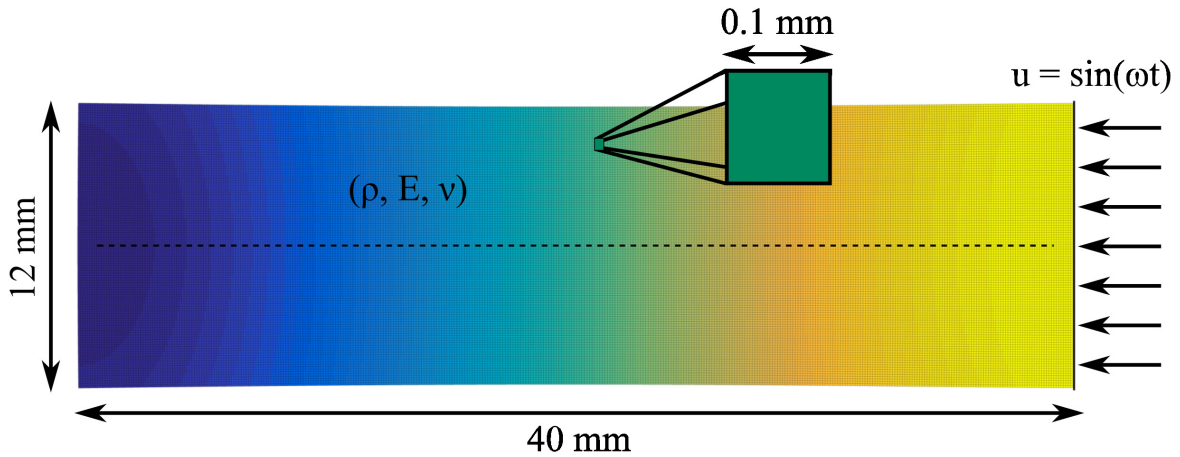


Fig. 11: Example of FE displacement field extracted at the top surface of the FE model and symmetrized along the transverse direction.

4.2 Synthetic grid deformation

The procedure used to evaluate the accuracy of the identification on real data is presented here. First, the sample deformation was simulated with the FE model described above. Then, synthetic grid images were numerically de-

formed using the FE displacements fields, grey level noise was added and the images were processed exactly as the experimental ones (see Section 2.4). The identified parameters can then be compared to the FE inputs and both systematic and random errors can be evaluated. A similar approach can be found in [33,32,38].

Synthetic and pixelated grids have been generated according to the following equation:

$$G(i, j) = \frac{\gamma}{4} \left(1 + \cos\left(2\pi \frac{i}{N}\right) \right) \left(1 + \cos\left(2\pi \frac{j}{N}\right) \right) + \tilde{\gamma} \quad (12)$$

with G is the pixelated grid, N is the spatial sampling (number of pixels per period) and γ and $\tilde{\gamma}$ characterises the image dynamic range (see Figure 12). A specific grid pitch p was also chosen to scale the image. In parallel, FE displacement fields were output from ANSYS and interpolated on the grid-mesh using a cubic spline interpolation. Such an interpolation is required to deform the grid using standard MATLAB libraries such as the *interp2* function. Finally, the grid was numerically deformed, assigning at grid location $M(i, j)$ an average of the grid grey level value around the location $M'(i + u, j + v)$ where u and v are the longitudinal and transversal FE displacement at that pixel location, respectively. Additional spline interpolations were required here to estimate the grey level value at locations $M'(i + u, j + v)$ and $M'(i + u \pm \varepsilon, j + v \pm \varepsilon)$, where ε is half the averaging window size. It corresponds to the field of view captured by one pixel of the camera, denoted *pix*, and allows taking into account the fact that a camera pixel only captures an average of the grid grey level over a certain physical domain. Here, this window was taken so that it covers the full pixel size, effectively simulating a fill factor of 100 %, while the Shimadzu HPV-X camera has a low fill factor, of the order of 40 %. Nevertheless, it was checked numerically that this effect could be neglected thanks to the very small recorded displacements (less than a third of a pixel), justifying the use of a 100 % fill factor here for the sake of simplicity and computing efficiency. Finally, a grey level Gaussian noise of standard deviation σ was added to the grid image to take into account the characteristic noise of the camera sensor. Such routine is applied to the initial grid image for different loading increments until reconstructing 127 synthetically deformed and noisy grid images comparable to the data set captured by the camera during a real experiment.

Figure 12c shows a zoomed in image of an experimental grid image and Figures 12a and 12b the grey level histogram and noise characteristics of the camera sensor. Figure 12c shows a zoom in of the synthetic grid after applying deformation and noise. The noise added to the synthetic images is based on Figure 12b where the standard deviation of the pixel noise (obtained from stationary images) for different pixels from dark to bright is plotted. The maximum noise was about 3.5 % of the pixel grey level and decreases as a function of the grey level intensity. The grid contrast has been selected to reproduce the histogram of Figure 12a. Comparing Figures 12c and 12d, one can note that the procedure detailed above describes reasonably well the grey level dynamic and the noise intensity. However,

the procedure does not take into account any grid defect and any fill-factor issues. Indeed, one observes in Figure 12c that the apparent pitch of the grid slightly varies along the horizontal direction. This is due to the fact that the pixel captures photons only over a small part of its physical domain (40 % for the HPV-X) which leads to a crop of the information especially visible in presence of sharp edges. Both these aspects have been neglected here.

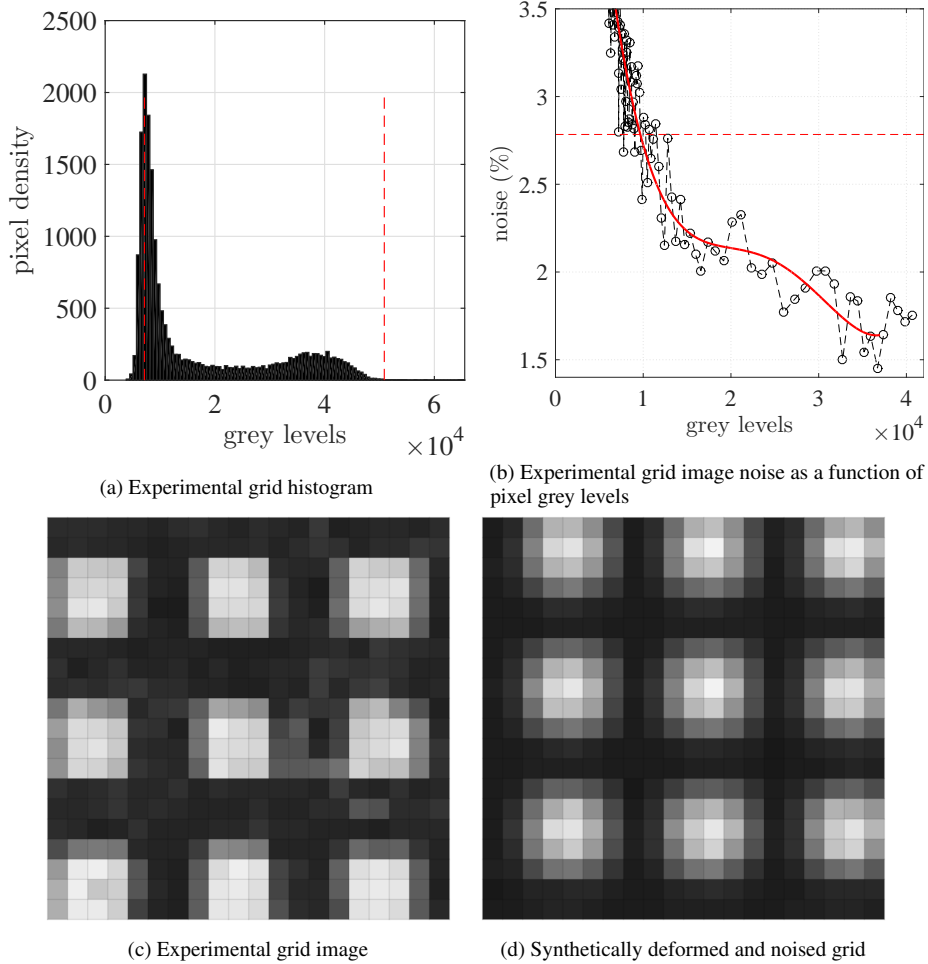


Fig. 12: Experimental images characteristics a), b) and zoom in views of an experimental and synthetic grid. The corresponding parameters are: $p = 1$ mm, $N = 7$ mm, $pix = 143$ μ m and $\sigma = 3.5$ %.

Before analysing the impact of the grid and camera parameters on the field reconstructions, one needs to choose a definition for the systematic and random errors, *i.e.* scalars accurately describing spatio-temporal deviations between input and output fields. The idea was to overcome two major problems: (1) the presence of infinite values in the definition of the relative error. It comes from the point-by-point division of the output fields by the input ones, of

which the local values can be null. (2) By smoothing the reconstructed displacement field, the random noise will be mitigated but outputs are more and more truncated which introduces low spatio-temporal frequency variations within the error. This makes it difficult to simply define the random error by the standard deviation of the relative error. The following two points are illustrated in Figures 13 where the relative error on displacement fields (see Eq. 13) and its random part (see Eq. 14) are presented for a simulated camera noise of 3.5 % with smoothing (Figures 13c and 13d) or without (Figures 13a and 13b). As expected, singular values close to the anti-node (sample centre) are present as well as for certain times when the signals go through zero. One can see the reduction of high frequency scatter when smoothing (from top to bottom) but also the creation of systematic low-spatial frequency variations (see Figure 13c). Based on these observations, it has been decided to define the systematic error, denoted ε^{syst} , as the median (over space and time) of the relative error field as the median is less sensitive to outliers arising from low signal points. The random error, denoted ε^{rand} , is defined as the standard deviation (over space and time) of the difference between the FE data corrected by the systematic error and the FE-grid data, normalized by the maximum of the signal in space and time. In equation format:

$$\varepsilon^{syst} = M_d \left[\frac{F^{FE}(x,t) - F^{grid}(x,t)}{F^{FE}(x,t)} \right] \quad (13)$$

$$\varepsilon^{rand} = s \left[\frac{F^{FE}(x,t)(1 - \varepsilon^{syst}) - F^{grid}(x,t)}{\max_{x,t}(F^{FE}(x,t))} \right] \quad (14)$$

where F^{FE} and F^{grid} are the FE (input) and post-processed (output) quantities of interest, $M_d[*]$ and $s[*]$ are the median and the standard deviation respectively. For the error on Young's modulus, the time has been removed from Eqs. 13 and 14 to calculate the error, as it does not depend on time.

Let us now look into the impact of the experimental spatial grid sampling, the temporal sampling and the camera sensor noise on measurements and identification. First, four different spatial grid pitches have been tested, namely $p = 0.7, 0.8, 0.9$ and 1 mm, and the error on kinematic quantities evaluated. No clear impact on the systematic error of displacement and strain has been identified since an error of $0.5^{\pm 0.1}\%$ on both displacement and strain has been found whatever the grid pitch. Therefore, the grid pitch chosen experimentally, 1 mm, has negligible impact on the displacement and strain. The reason for this is certainly the low spatial frequency contents of the deformation when the material undergoes deformation at its first longitudinal mode. Deforming the material at higher deformation modes, or using a strain concentrator like a notch or a hole, would require to run this check again.

Then, five different frame rates have been used, namely $f = 0.2, 0.5, 1, 2$ and 5 Mfps, on a 1 mm pitch grid. Table 3 summarizes the results.

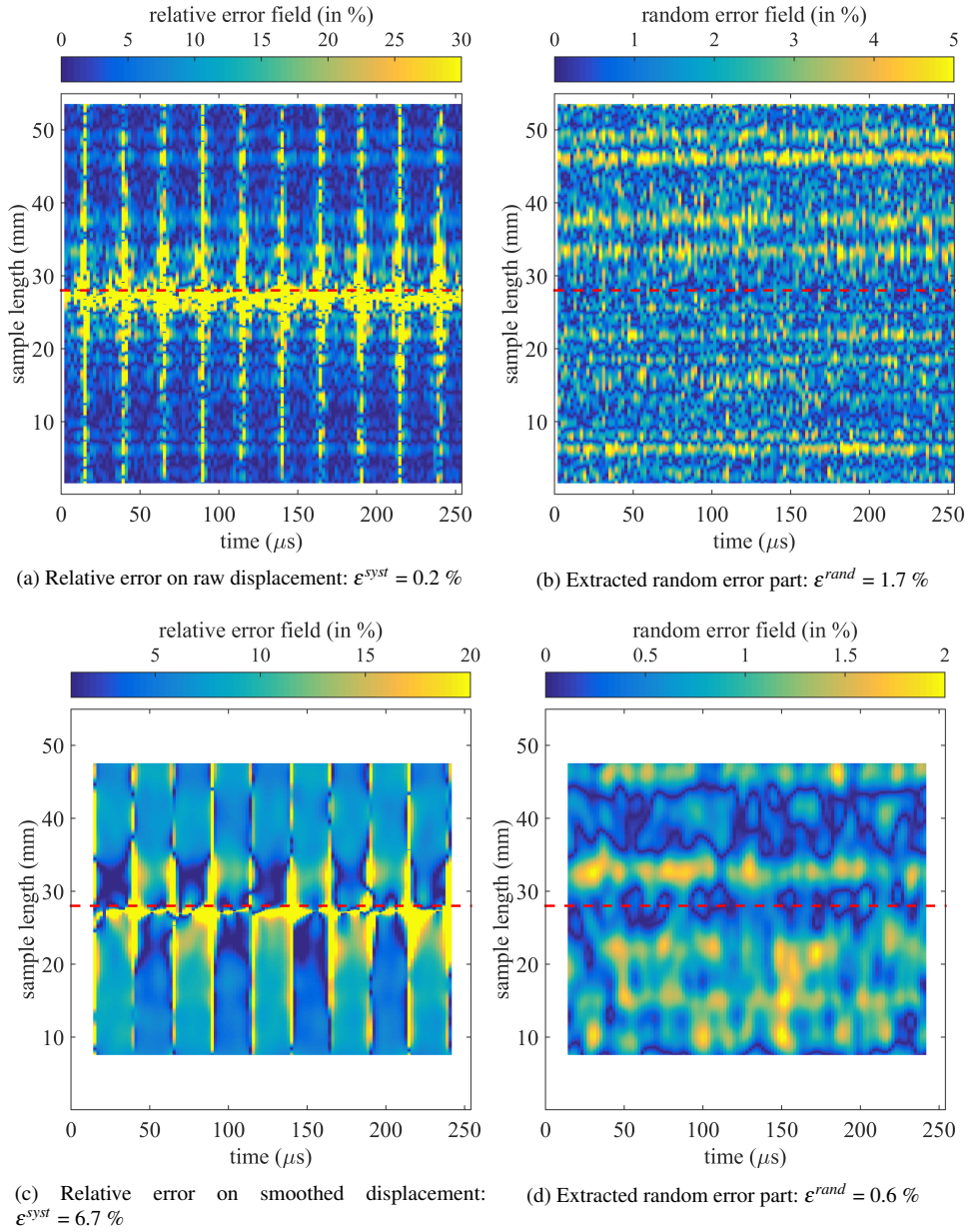


Fig. 13: Spatio-temporal displacement error maps. On the left column is the absolute value of the relative error and on the right column is the absolute value of the extracted random part. The corresponding parameters are: $p = 1$ mm, $N = 7$ mm, $pix = 143 \mu m$, $\sigma = 3.5 \%$ and smoothing kernel $s = 7$.

One observes that only the 0.2 Mfps frame rate significantly affects the results. Indeed, an error of about 12 % is found for simulation recorded at 0.2 Mfps, while only 1-2 % of error was found for higher frame rates. This confirms the choice of 0.5 Mfps for the experiments, and also shows that a slight improvement would have been obtained recording at 1 Mfps or more. It is interesting to notice that the small unexpected increase of the identification error over

	Frame rate (Mfps)				
	0.2	0.5	1	2	5
Accel. (finite diff.)	11.6	0.9	0.7	1.1	1.2
Accel. (harm.)	0.3 →				
Stress (finite diff.)	11.4	0.7	1.0	1.7	1.9
Stress (harm.)	0.14 →				
Young's modulus (finite diff.)	12.3	1.9	0.3	0.5	1.2
Young's modulus (harm.)	0.5 →				

Table 3: Systematic error (in %) between FE and synthetic grid deformation data, for different frame rates. The grid pitch is 1 mm and the displacement amplitude is $\pm 30 \mu m$.

1 Mfps is probably due to the fact that the systematic errors presented here are based on spatio-temporal data obtained considering a constant number of frames captured by the camera (128) and not considering a constant number of deformation cycles. This has been chosen to be in line with the physical limitation of the camera. In other words, when an increase of the acquisition frequency is simulated, a decrease of the number of captured deformation cycles occurs. At 1 Mfps, two and a half cycles are captured, at 2 Mfps only one and at 5 Mfps, only half of a cycle. Therefore, increasing the frame rate affects the consistency of the comparison and probably slightly increases the systematic error. However, this error still remains very small. The table also shows that avoiding temporal differentiation by using the harmonic assumption leads to lower errors on the acceleration and stress, as expected.

Finally, a noise level of 3.5 % was added to the synthetically deformed grid images, each of the 128 images bearing a different copy of the noise. Table 4 and Figure 14 present how displacement smoothing affects the strain, acceleration, stress and identified Young's modulus. For comparison, Figures 13 provide the error fields corresponding to the first row, column one and two in Table 4. The first column of Table 4 shows the level of noise before any post-smoothing. No systematic error is observed but a significant random error can be seen on differentiated quantities, especially the strain and the acceleration with a noise standard deviation of about 11 % and 13 %, respectively. One can see that the random error level is only about 6 % on stress (finite diff.). This point is in line with the fact that the stress comes from averaging the acceleration between each material section and the free edge. This is a regularizing process. In addition, one observes that the harmonic assumption significantly mitigates the influence of the noise. Both harmonic acceleration and stress have a level of noise similar to the displacement one. Finally, one can see that the identified Young's modulus has a systematic error which is about twice as large when using finite differences instead of the harmonic assumption to derive the acceleration. The latter is therefore favoured, as expected.

Table 4, column two, focuses on the smoothing kernel size selected for the treatment of the experimental data. A kernel size of 7 was applied in space to derive the strains, and in time to derive the acceleration using finite

	no smoothing	smoothed k = 7
Displacement	0.2 \pm 1.7	6.7 \pm 0.6
Strain	0.4 \pm 11.0	6.7 \pm 2.7
Acc. (finite diff.)	0.6 \pm 12.9	7.2 \pm 1.5
Acc. (harm.)	0.2 \pm 1.7	6.7 \pm 0.6
Stress (finite diff.)	0.1 \pm 5.7	7.0 \pm 1.2
Stress (harm.)	0.2 \pm 1.0	6.6 \pm 0.8
Young's modulus (finite diff.)	2.8 \pm 3.1	1.4 \pm 1.8
Young's modulus (harm.)	1.5 \pm 3.2	0.8 \pm 1.8

Table 4: Systematic and random errors (in %) between FE and synthetic grid deformation data. The image noise was 3.5 % of the grey level value and the displacement amplitude $\pm 30 \mu m$. Smoothing was Gaussian with kernel k , in space for strains, and in time for acceleration (finite difference). Data provided as systematic \pm random error.

differences. Two things can be noticed: first, smoothing the data introduces a systematic error of the order of 7 % for all quantities except the identified Young's modulus. Second, it significantly reduces the random error for the differentiated quantities, *i.e.* the strain (-8 %), the acceleration (-11 %) and the stress (-4.5 %). As expected, the random error does not reduce significantly on acceleration and stress when using the harmonic assumption, the smoothing just increasing the systematic error. The situation for Young's modulus is somewhat unexpected as not only does the random error decrease, as expected, but also the systematic error by a factor of two. This comes from the fact that both stress and strain systematic errors cancel out when the modulus is calculated. Whether this is a general result or just a fortunate fact arising from the precise set of smoothing parameters used here remains to be confirmed.

Finally, Figure 14 shows the variation of the systematic and random errors when the smoothing kernel size varies. For all quantities, the systematic error increases when the smoothing kernel increases and the random error decreases when the kernel increases, as expected. This allows to select the smoothing in a rational way to minimize the total error, as in [38]. It is clear from Figures 14b, 14c and 14e that a smoothing kernel between 5 and 7 is recommended. Regarding the identified Young's modulus, it is interesting to notice that the trend of the systematic error is almost flat whereas the systematic error on both strain and stress increases as a function of smoothing kernel size. It means that the systematic errors on both stress and strain increase in similar ways and cancel out in the Young's modulus identification. This specific point means that depending on the purpose of the study, *i.e.* identifying a material parameter or measuring accurately mechanical quantities, the choice of the smoothing kernel will not necessarily be the same. In parallel, one observes that the random error on Young's modulus identification significantly decreases over a smoothing window of 5. Nevertheless, none of the tested parameters allow reaching an error level below 1 %. A wider range of smoothing and grid parameters would be needed to better understand this, but this was beyond the scope of the present validation which focuses on evaluating the expected error for the parameters used in the experimental study. These results also demonstrate the benefit of the synthetic image deformation pro-

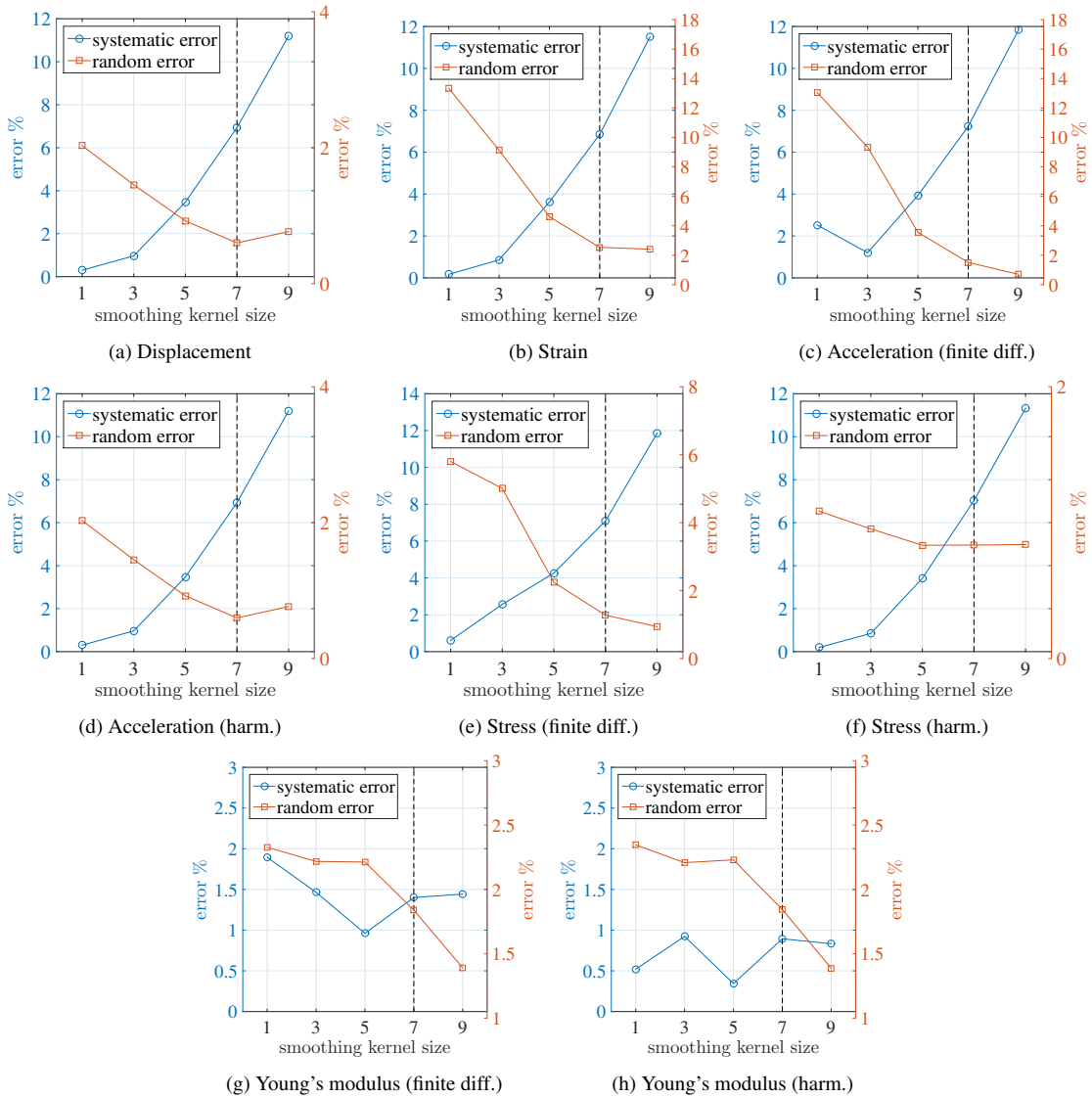


Fig. 14: Systematic and random errors (in %) between FE and synthetic grid deformation data. The image noise was 3.5 % of the grey level value and the displacement amplitude $\pm 30 \mu m$.

cess to gain insight into the errors than can be expected on the identified quantities, as already pointed out in [38,32,33].

To conclude, Figure 15 presents the relative error expected on Young's modulus identification for the experimental conditions presented in Section 3, *i.e.* a grid pitch of 1 mm, a frame rate of 0.5 Mfps, a flat camera sensor noise across pixel grey level values of 3.5 % and a data post-smoothing kernel of 7 prior to both spatial and temporal differentiation. In view of the simplifications in the FE model, in particular the fact the material does not include any viscoelastic effects, *i.e.* no Young's modulus variations along the sample length are present, the results can be seen as a lower

bound of the identification error. Figure 15a presents the relative error on the identified Young's modulus all along the sample length. The dotted red line represents the median value already reported in Table 4. One observes a 3 % oscillation of the identified Young's modulus along the sample length, from 10 to 40 mm. Between 5 and 10 mm, and 40 and 50 mm, oscillations reach 10 %. Close to the free (0 mm) and the loaded (55 mm) edges, the identification error shoots up. This is due to the fact that both stresses and strains are zero at the deformation nodes. It is worth noting that the sample extremities (one smoothing kernel, i.e. 7 data, at both ends) have not been taken into account for the estimation of the systematic and random errors presented within this section. Such a figure shows that the accuracy of the identification is not constant over the sample length and depends on the position of the material section compared to the deformation nodes and anti-nodes. Indeed, Figure 15 presents a characteristic *U* shape which derives from the spatial variation of the signal to noise ratio. Here, the spatial location can be translated into strain-rate in order to underline the resulting impact of such signal to noise ratio variation on the ability to the experiment to characterize mechanical properties at lower strain-rate.

Figure 15b presents the relative error on the identified Young's modulus as a function of the strain-rate amplitude seen by each sample section. One clearly sees that the relative error on Young's modulus starts from 1 % at maximum strain-rate (i.e. sample centre) then gradually increases as the considered section gets closer to the edges. Within the domain $[200-250] \text{ s}^{-1}$, the systematic error remains below 2 % and reaches 6 % down to 90 s^{-1} . Below this, Young's modulus is not identified accurately anymore. Such observations are in line with the experimental observations. Indeed, Figure 10a shows an identification scatter about $\pm 5 \%$ at the sample centre (high temperature - high strain-rate) and about $\pm 10 \%$ close to sample edge which is consistent with Figure 15b. Moreover, Figure 15b shows that the systematic error slightly increases close to the sample edges which could partially explain the deviation with [30], observed in Figure 10a at 10^2 s^{-1} .

The present data lead to the following conclusions. (1) Combining a spatially heterogeneous loading together with kinematic and temperature full-field measurements, it is possible to identify Young's modulus over a certain range of thermo-mechanical loading conditions. (2) The accuracy of the local identification strongly depends on experimental conditions and processing parameter selection, especially the sensor noise, the acquisition frequency, the camera resolution, the grid resolution and the smoothing parameters. Such parameters can be chosen in a rational way by combining finite element modelling and synthetic grid deformation. (3) Nevertheless, with such a "one-shot" technique, the cost to pay is a variation of the signal to noise ratio as a function of spatial location, i.e. also as a function of temperature, strain and strain-rate. Here, the results are acceptable down to strain-rates of 90 s^{-1} and

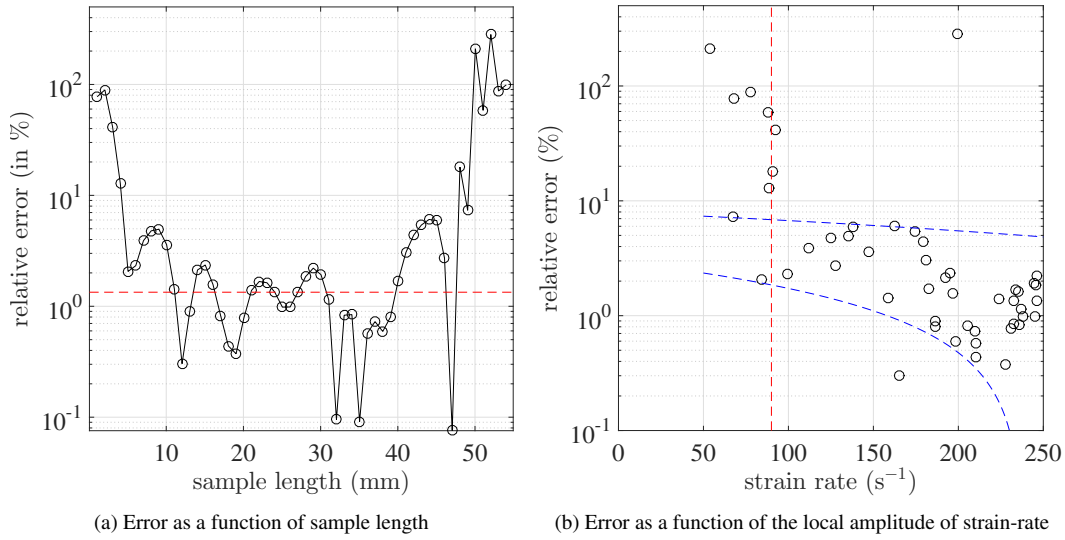


Fig. 15: Absolute value of the relative error on Young's modulus identification for a grid pitch of 1 mm, a temporal sampling $f = 0.5$ Mfps, a grid noise of 3.5 % and a spatio-temporal smoothing kernel size of 7^2 . The material was assumed, isotropic, homogeneous and purely elastic. The displacement amplitude is $\pm 30 \mu\text{m}$ and the acceleration was obtained from finite difference. The red line in a) is the median value while the red line in b) underlines the limit (90 s^{-1}) under which the identification error shoots up.

up to 250 s^{-1} . Deeper investigations using thermo-mechanical viscoelastic simulations are required to gain better understanding of the metrological limitations of the experiment.

5 Outstanding issues and scope of the method

Although the feasibility of a "one-shot" time-dependent properties identification has been demonstrated on a PMMA sample and the results are in good agreement with data obtained from other methods, such as DMTA and high-speed compressive tests, it is important to understand the limitations and outstanding issues of the proposed methodology. A few points need to be raised.

- **The difficulty to clearly define an apparent strain-rate.** Such difficulty is actually also present in DMTA and SPHB tests but at least the methodologies are consistent since data are also averaged in space. In the present case, the following issue can introduce a horizontal shift of the data in Figure 9. As the strain-rate for result reported here is the maximum strain-rate, effective properties may be slightly shifted towards lower strain-rates. One can notice that the convention in DMTA is to approximate the strain-rate by $\dot{\epsilon} = 4f\epsilon_{max}$ [24] whereas one uses here $\dot{\epsilon}_{max}$, i.e. $\approx 2\pi f\epsilon_{max}$ which would lead to an horizontal shift of about 0.2 s^{-1} . This is not enough to explain the significant differences observed in Figure 10b.

- **The strain amplitude sensitivity.** The strain varies along the sample length and during the test from 0.01 to 0.35 %, which means that the following test is close to DMTA in term of deformation amplitude (0.1 %) but somewhere between hydraulic machine tests and SHPB tests in term of strain-rates. The potential impact of the strain amplitude on the storage modulus variation, especially at low strains, is not clear and could introduce some variation of storage modulus simply due to strain amplitude variations. This point can affect the global shape of the master curve.
- **Limitation of a 1D approach.** It has been observed that the temperature was not perfectly uniform over a material section (see supplementary data) due to both higher heat losses at the edges and unsymmetrical strain localization. It seems important to investigate how such an approach could be extended to a 2D case which would not require this assumption. The present authors are currently working on a strategy based on the use of the Virtual Fields Method and a subset-based equilibrium to overcome such an issue.

While the current article focuses on a rather simple application (a homogeneous rectangular specimen in the elastic regime) as a first demonstrator, the present strategy has great potential for a range of problems not addressed with current test methods.

1. **Fracture of brittle materials at high strain-rate.** Brittle materials like glass or concrete are notoriously difficult to test at high rates of strain. A preliminary numerical simulation on glass with a $\pm 60 \mu m$ excitation amplitude (limit of the current ultrasonic excitation system), and considering a very low damping coefficient of $\beta \approx 10^{-9}$ leads to a maximum stress of $\sigma = \pm 95 MPa$, i.e. about the fracture stress of glass. As the material is not damped, the actuator can work over its whole displacement range to reach the failure stress of glass. Combining such test with a 2D generalization of the method would allow characterizing glass failure at high strain-rates. An initial experimental proof of principle has been conducted and a glass specimen has been successfully fractured.
2. **Transverse fracture of composites.** Because of the very low failure stress of a unidirectional (UD) composite in the direction transverse to the fibres, its tensile fracture stress is very difficult to obtain using SHPB experiments. A preliminary finite element study showed that an amplitude of $\pm 100 \mu m$ would be required to reach $\sigma = 50 MPa$ with $E = 10 GPa$ and $\beta \approx 10^{-8}$. While this is larger than what the current system used here can provide, it is not impossible to reach. An alternative could also be to fix a mass at the free end, this would however require a significant numerical test design campaign. The situation is even more difficult for the through thickness tensile properties where very small specimens have to be used. In this case, a thin laminate could be sandwiched between two steel blocks and displacement measurements just performed on the steel blocks with a direct reading to the transverse stress from the free end steel block.
3. **Adhesives.** The same idea as for the through-thickness composites test could be employed for adhesives which are notoriously difficult to test at high rates [39].

4. **Yielding of engineering alloys.** From initial finite element simulations, the actuator would also need an amplitude of $\pm 160 \mu\text{m}$ to yield an aluminium sample (with $\sigma_y = 280 \text{ MPa}$, $E = 72 \text{ GPa}$ and $\beta \approx 10^{-10}$). Again, this is too large for the current setup but a specific horn could be designed to boost the excitation amplitude further.
5. **Extended strain-rate range.** The current strain-rate range is imposed by the excitation frequency, the strain concentration within the sample and the covered range of temperatures (considering time-temperature superposition). It is possible to reach higher apparent strain-rates by cooling down the sample prior to the start of the test, *e.g.* building a temperature controlled enclosure. According to preliminary calculations and tests, cooling the specimen down to 10°C only would allow reaching the equivalent of 10^3 s^{-1} at room temperature, while cooling down to -10°C would allow reaching 10^4 s^{-1} at room temperature for PMMA samples. Working on sample geometry (using notches for instance) would lead to strain concentrations and thus higher local strain-rates. Nevertheless, the suitability of the low spatial resolution camera would need to be verified, and the 1D approach would most probably not be enough.
6. **Heterogeneous materials.** Although the present paper uses a simple homogeneous PMMA specimen for the sake of validation of the test concept, it is clear that the main asset of this image-based DMTA is to investigate heterogeneous materials. Indeed, while a technique such as DMTA is now well mastered and allows capturing the behaviour of rheologically simple materials over a very large range of strain-rates (see Figure 10b), it cannot provide spatial maps of properties and therefore, cannot derive detailed properties for heterogeneous materials. An interesting case for instance could be injected polymeric sheets which have different properties in the skin than in the core. The present method has the potential to provide spatially-resolved properties.

These opportunities will be studied in more depth by the current authors in the near future.

6 Conclusion

The present work demonstrates the feasibility of a multi-parametric identification on a single sample and falls within an effort to invent new high-strain test methodologies based on full-field imaging and inverse identification, to both overcome the limits of standard experimental strategies and take advantage of the deformation heterogeneities to achieve a full-characterization of a material from a "one-shot" test. It has been demonstrated that using a 20 kHz high power ultrasonic excitation combined with infrared thermography and ultra-high speed imaging, a PMMA sample could be subjected to apparent strain-rates varying from less than 10^0 s^{-1} to 10^2 s^{-1} and temperatures varying from ambient to its T_g . Within the studied strain-rate range, a significant increase in storage modulus has been evidenced that was not visible in the DMTA results. This interesting observation justifies the interest in developing new measurement techniques to capture the material behaviour at intermediate and high strain-rates. The validity of the approach has been checked using Finite Element modelling combined with synthetic grid image deformation. It demonstrates, under

simple behaviour assumptions, that the error on identification is expected to remain below 10 % over the sample length. This has been partially confirmed by the experimental data scatter. Finally, the potential of this new test technique has been underlined and it is expected that it will evolve to join the toolkit of researchers and engineers in mechanics of materials.

7 Acknowledgement and funding

This material is based on research sponsored by the Air Force Research Laboratory, under agreement number FA9550-15-1-0293. The U.S. Government is authorized to reproduce and distribute reprints for Governmental purposes notwithstanding any copyright notation thereon. The views and conclusions contained herein are those of the authors and should not be interpreted as necessarily representing the official policies or endorsements, either expressed or implied, of the Air Force Research Laboratory or the U.S. Government. The authors would like to thank Dr Jason Foley (AFOSR), Dr Matt Snyder (EOARD) and Dr David Garner (EOARD) for supporting this work.

Prof. Pierron acknowledges funding from EPSRC through grant EP/L026910/1, as well as from the Wolfson Foundation through a Royal Society Wolfson Research Merit Award.

The authors are also grateful to Prof. Clive Siviour from the Department of Engineering Science at the University of Oxford for providing the DMTA results and for helpful discussions.

The authors are also grateful to Dr. Frances Davis from the Engineering and the Environment research group from the University of Southampton for performing the quasi-static tests, density measurements and DSC analysis on PMMA samples, as well as for helpful discussions.

All data supporting this study are openly available from the University of Southampton repository at <http://doi.org/10.5258/SOTON/D0207>

References

1. J. Capodagli and R. Lakes. Isothermal viscoelastic properties of PMMA and LDPE over 11 decades of frequency and time: a test of time–temperature superposition. *Rheologica Acta*, 47(7):777–786, 2008.
2. J. Crooks, B. Marsh, R. Turchetta, K. Taylor, W. Chan, A. Lahav, and A. Fenigstein. Kirana: A solid-state megapixel ucmos image sensor for ultrahigh speed imaging. In *Proceedings of SPIE - The International Society for Optical Engineering*, volume 8659, 2013.
3. S. Dreuilhe, F. Davis, C. R. Siviour, and F. Pierron. Image-based inertial impact tests on an aluminum alloy. In *Conference Proceedings of the Society for Experimental Mechanics Series*, volume 3, pages 219–223, 2016.
4. S. Dreuilhe and F. Pierron. Extension of the non-linear virtual fields method to inertial heterogeneous high strain rate tests. *Conference Proceedings of the Society for Experimental Mechanics Series*, 4:83–87, 2015.
5. J. E. Field, S. M. Walley, W. G. Proud, H. T. Goldrein, and C. R. Siviour. Review of experimental techniques for high rate deformation and shock studies. *International Journal of Impact Engineering*, 30(7):725–775, 2004.

6. R. Fruehmann, D. Crump, and J. Dulieu-Barton. Characterization of an infrared detector for high frame rate thermography. Measurement Science and Technology, 24(10):105403, 2013.
7. A. Giraudeau, F. Pierron, and B. Guo. An alternative to modal analysis for material stiffness and damping identification from vibrating plates. Journal of Sound and Vibration, 329(10):1653–1672, 2010.
8. M. Grédiac, N. Fournier, P. A. Paris, and Y. Surrel. Direct identification of elastic constants of anisotropic plates by modal analysis: Experimental results. Journal of Sound and Vibration, 210(5):643–659, 1998.
9. M. Grédiac and P. A. Paris. Direct identification of elastic constants of anisotropic plates by modal analysis: Theoretical and numerical aspects. Journal of Sound and Vibration, 195(3):401–415, 1996.
10. M. Grédiac, F. Sur, and B. Blaysat. The grid method for in-plane displacement and strain measurement: A review and analysis. Strain, 52(3):205–243, 2016.
11. J. Halary, A. Oultache, J. Louyot, B. Jasse, T. Sarraf, and R. Muller. Viscoelastic properties of styrene-co-methyl methacrylate random copolymers. Journal of Polymer Science Part B: Polymer Physics, 29(8):933–943, 1991.
12. M. J. Kendall and C. R. Siviour. Experimentally simulating high rate composite deformation in tension and compression: polymer bonded explosive simulant. Journal of Dynamic Behavior of Materials, 1(2):114–123, 2015.
13. B. Koohbor, A. Kidane, and W.-Y. Lu. Characterizing the constitutive response and energy absorption of rigid polymeric foams subjected to intermediate-velocity impact. Polymer Testing, 54:48–58, 2016.
14. B. Koohbor, A. Kidane, and W.-Y. Lu. Effect of specimen size, compressibility and inertia on the response of rigid polymer foams subjected to high velocity direct impact loading. International Journal of Impact Engineering, 98:62–74, 2016.
15. B. Koohbor, A. Kidane, W.-Y. Lu, and M. A. Sutton. Investigation of the dynamic stress–strain response of compressible polymeric foam using a non-parametric analysis. International Journal of Impact Engineering, 91:170–182, 2016.
16. B. Koohbor, A. Kidane, W.-Y. Lu, and M. A. Sutton. Investigation of the dynamic stress-strain response of compressible polymeric foam using a non-parametric analysis. International Journal of Impact Engineering, 2016.
17. B. Koohbor, S. Mallon, A. Kidane, and W.-Y. Lu. The deformation and failure response of closed-cell pmdi foams subjected to dynamic impact loading. Polymer Testing, 44(0):112–124, 2015.
18. R. S. Lakes. Viscoelastic solids, volume 9. CRC press, 1998.
19. G. Le Louédec, F. Pierron, M. A. Sutton, C. Siviour, and A. P. Reynolds. Identification of the dynamic properties of al 5456 fsw welds using the virtual fields method. Journal of Dynamic Behavior of Materials, 1(2):176–190, 2015.
20. Z. Li and J. Lambros. Strain rate effects on the thermomechanical behavior of polymers. International Journal of Solids and Structures, 38(20):3549–3562, 2001.
21. B. Lukić, D. Saletti, and P. Forquin. Use of simulated experiments for material characterization of brittle materials subjected to high strain rate dynamic tension. Philosophical Transactions of the Royal Society A: Mathematical, Physical and Engineering Sciences, 375(2085), 2017.
22. R. Moulart, F. Pierron, S. Hallett, and M. Wisnom. High strain rate photomechanics on composites: use of a ultra high speed camera and the virtual fields method. In P. C. A. Rusinek, editor, Workshop in memory of J.R. Klepaczko, 2009.
23. R. Moulart, F. Pierron, S. R. Hallett, and M. R. Wisnom. Full-field strain measurement and identification of composites moduli at high strain rate with the virtual fields method. Experimental Mechanics, 51(4):509–536, 2011.
24. A. Mulliken and M. Boyce. Mechanics of the rate-dependent elastic–plastic deformation of glassy polymers from low to high strain rates. International journal of solids and structures, 43(5):1331–1356, 2006.
25. F. Pierron. Addendum to ‘Characterising the strain and temperature fields in a surrogate bone material subject to power ultrasonic excitation’. Strain, 52(3):186–190, 2016.

26. F. Pierron and P. Forquin. Ultra-high-speed full-field deformation measurements on concrete spalling specimens and stiffness identification with the virtual fields method. *Strain*, 48(5):388–405, 2012.
27. F. Pierron, H. Zhu, and C. Siviour. Beyond Hopkinson’s bar. *Philosophical Transactions of the Royal Society of London A: Mathematical, Physical and Engineering Sciences*, 372(2023):20130195, 2014.
28. J.-L. Piro and M. Grédiac. Producing and transferring low-spatial-frequency grids for measuring displacement fields with moiré and grid methods. *Experimental Techniques*, 28(4):23–26, 2004.
29. P. L. Reu and T. J. Miller. The application of high-speed digital image correlation. *Journal of Strain Analysis for Engineering Design*, 43(8):673–688, 2008.
30. J. Richeton, G. Schlatter, K. Vecchio, Y. Rémond, and S. Ahzi. A unified model for stiffness modulus of amorphous polymers across transition temperatures and strain rates. *Polymer*, 46(19):8194–8201, 2005.
31. A. Robinson, J. Dulieu-Barton, S. Quinn, and R. Burguete. Paint coating characterization for thermoelastic stress analysis of metallic materials. *Measurement Science and Technology*, 21(8):085502, 2010.
32. M. Rossi, P. Lava, F. Pierron, D. Debruyne, and M. Sasso. Effect of dic spatial resolution, noise and interpolation error on identification results with the vfm. *Strain*, 51(3):206–222, 2015.
33. M. Rossi and F. Pierron. On the use of simulated experiments in designing tests for material characterization from full-field measurements. *International Journal of Solids and Structures*, 49(3):420–435, 2012.
34. R. Seghir, J.-F. Witz, L. Bodelot, E. Charkaluk, and P. Dufrénoy. An improved lagrangian thermography procedure for the quantification of the temperature fields within polycrystals. *Quantitative InfraRed Thermography Journal*, 10(1):74–95, 2013.
35. M. A. Sutton, J. J. Orteu, and H. W. Schreier. Image correlation for shape, motion and deformation measurements: Basic concepts, theory and applications. *Image Correlation for Shape, Motion and Deformation Measurements: Basic Concepts, Theory and Applications*, pages 1–321, 2009.
36. Y. Tochigi, K. Hanzawa, Y. Kato, R. Kuroda, H. Mutoh, R. Hirose, H. Tominaga, K. Takubo, Y. Kondo, and S. Sugawa. A global-shutter cmos image sensor with readout speed of 1-tpixel/s burst and 780-mpixel/s continuous. *IEEE Journal of Solid-State Circuits*, 48(1):329–338, 2013.
37. D. Wang, M. Lucas, and K. Tanner. Characterising the strain and temperature fields in a surrogate bone material subject to power ultrasonic excitation. *Strain*, 49(5):409–419, 2013.
38. P. Wang, F. Pierron, M. Rossi, P. Lava, and O. T. Thomsen. Optimised experimental characterisation of polymeric foam material using dic and the virtual fields method. *Strain*, 52(1):59–79, 2016.
39. T. Yokoyama and K. Nakai. Determination of the impact tensile strength of structural adhesive butt joints with a modified split hopkinson pressure bar. *International Journal of Adhesion and Adhesives*, 56:13–23, 2015.
40. S.-h. Yoon, I. Giannakopoulos, and C. R. Siviour. Application of the virtual fields method to the uniaxial behavior of rubbers at medium strain rates. *International Journal of Solids and Structures*, 69-70:553–568, 2015.
41. S.-h. Yoon, M. Winters, and C. R. Siviour. High strain-rate tensile characterization of epdm rubber using non-equilibrium loading and the virtual fields method. *Experimental Mechanics*, 56(1):25–35, 2016.

Appendix

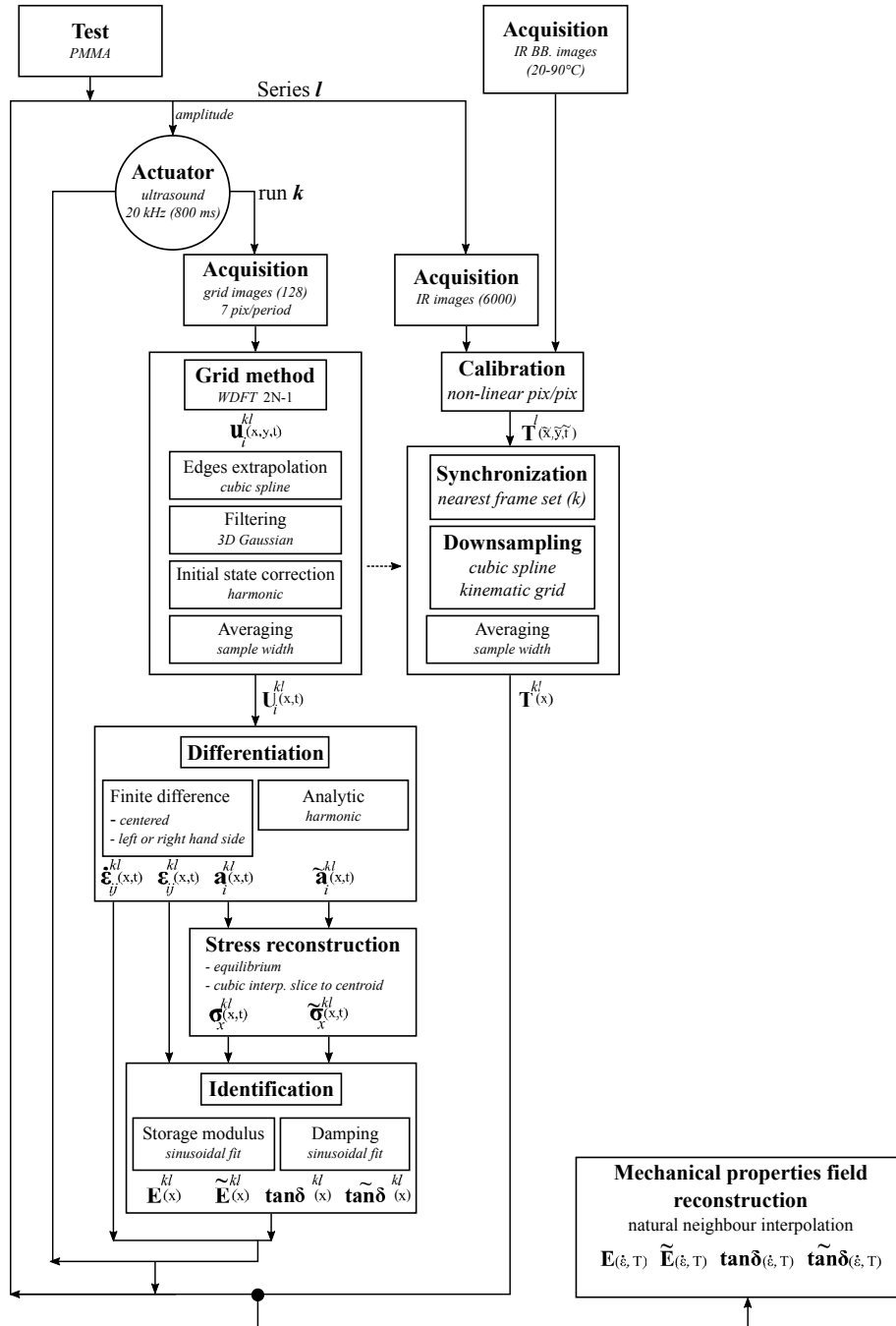


Fig. 16: Data post-processing procedure